

Hubble Space Telescope astrometry of the closest brown dwarf binary system. I. Overview and improved orbit^{*}

L. R. Bedin^{1†}, D. Pourbaix^{2‡}, D. Apai^{3,4}, A. J. Burgasser⁵, E. Buenzli⁶,
H. M. J. Boffin⁷, and M. Libralato^{1,8,9§}

¹*INAF-Osservatorio Astronomico di Padova, Vicolo dell'Osservatorio 5, I-35122 Padova, Italy*

²*Institut d'Astronomie et d'Astrophysique, Université Libre de Bruxelles (ULB), 1050 Bruxelles, Belgium*

³*Department of Astronomy and Steward Observatory, The University of Arizona, 933 N. Cherry Avenue, Tucson, AZ 85721, USA*

⁴*Lunar and Planetary Laboratory, The University of Arizona, 1640 E. University Blvd., Tucson, AZ 85721, USA*

⁵*Center for Astrophysics and Space Science, University of California San Diego, La Jolla, CA 92093, USA*

⁶*Institute for Astronomy, ETH Zurich, Wolfgang-Pauli-Strasse 27, 8093 Zurich, Switzerland*

⁷*European Southern Observatory, Karl Schwarzschild Strasse 2, D-85748 Garching, Germany*

⁸*Space Telescope Science Institute, 3800 San Martin Drive, Baltimore, MD 21218, USA*

⁹*Dipartimento di Fisica e Astronomia, Univ. di Padova, Vicolo dell'Osservatorio 3, I-35122 Padova, Italy*

Accepted 2017 May 9. Received 2017 May 9; in original form 2017 April 13

ABSTRACT

Located at 2 pc, the L7.5+T0.5 dwarfs system WISE J104915.57–531906.1 (Luhman 16 AB) is the third closest system known to Earth, making it a key benchmark for detailed investigation of brown dwarf atmospheric properties, thermal evolution, multiplicity, and planet-hosting frequency. In the first study of this series – based on a multi-cycle *Hubble Space Telescope* (*HST*) program – we provide an overview of the project and present improved estimates of positions, proper motions, annual parallax, mass ratio, and the current best assessment of the orbital parameters of the A-B pair. Our *HST* observations encompass the apparent periastron of the binary at 220.5 ± 0.2 mas at epoch 2016.402. Although our data seem to be inconsistent with recent ground-based astrometric measurements, we also exclude the presence of third bodies down to Neptune masses and periods longer than a year.

Key words: astrometry – binaries: visual – brown dwarfs.

1 INTRODUCTION

The first completeness-corrected planet occurrence rates emerging from the *Kepler* mission reveal a larger number of short-period Earth-sized planets around M dwarfs than around earlier-type (FGK) stars (Dressing & Charbonneau 2013, Fressin et al. 2013). Combined with state-of-the-art planet radius–mass relationships, studies indicate that there are about $3.5\times$ as many $1-4 M_{\text{Earth}}$ mass planets around M-type stars than around G-type stars, with a period-dependence on planet occurrence rate that varies monotonically with host spectral types (Mulders et al. 2015). The larger number of small planets around M-dwarfs con-

tains *more* mass in solids than the same small planet population around G-type stars (Mulders et al. 2016). Given that discs around higher-mass stars have higher masses (e.g., Pascucci et al. 2016), the higher occurrence rates and higher solid mass of small planets around lower-mass stars may be the result of inward migration of planets or their planetary building blocks. The recent discovery of seven approximately Earth-sized planets in the TRAPPIST-1 system (a star at the stellar/substellar boundary) provides a striking demonstration of the high occurrence rates of small planets around small stars (Gillon et al. 2017).

These results motivate studies of the small planet population around even lower-mass hosts, the brown dwarfs (BDs, Kumar 1962, Hayashi & Nakano 1963). These low-mass objects, incapable of hydrogen fusion, also host circumstellar discs (e.g., Luhman et al. 2008) which evolve through the first steps of planet formation (e.g., Apai et al. 2005, Pascucci et al. 2009, Ricci et al. 2013). However, planet detection through radial velocity (RV), transit, and high-contrast imaging are not effective for BD primaries due

^{*} Based on observations with the NASA/ESA *Hubble Space Telescope*, obtained at the Space Telescope Science Institute, which is operated by AURA, Inc., under NASA contract NAS 5-26555, under GO-13748 and GO-14330.

[†] E-mail: luigi.bedin@oapd.inaf.it

[‡] Senior Research Associate, F.R.S.-FNRS, Belgium.

[§] Starting a Post.Doc at STScI on July 1st, 2017

to their low luminosities ($<10^{-3} L_{\odot}$; Burrows et al. 2001). In contrast, high-precision astrometric observations have the potential to provide an extremely sensitive assessment of the presence of planets and to constrain the orbital inclination of the planetary system.

The *Wide-field Infrared Survey Explorer (WISE)* has discovered many of the nearest BDs in the Solar neighbourhood ($d < 20$ pc). A key example is WISE J104915.57–531906.1 AB, identified by Luhman (2013) as a binary BD located 2 pc from the Sun (hereafter Luhman 16 AB to follow the Burgasser et al. 2013 denomination). Luhman 16 A and B orbit each other at a distance of a few Astronomical Units with an orbital period of decades. As the closest known BDs, the system is ideally suited for detailed characterization.

The primary (Luhman 16 A) is of spectral type L7.5 \pm 1 and the secondary (Luhman 16 B) of type T0.5 \pm 1.5. Both at effective temperatures of about 1,300 K, placing them near the L-T transition (Luhman 2013, Burgasser et al. 2013; Kniazev et al. 2013; Faherty et al. 2014; Lodieu et al. 2015). The system age is constrained to about 0.1-3 Gyr, implying masses below $0.06 M_{\odot}$ (Faherty et al. 2014, Lodieu et al. 2015). There is no evidence for the pair belonging to any nearby young moving group (Mamajek 2013, Lodieu et al. 2015). Both brown dwarfs are known variables, with the B component more strongly variable than A. The variability likely originates from patchy clouds (Gillon et al. 2013, Crossfield et al. 2014, Buenzli et al. 2014, 2015a, Karalidi et al. 2016).

Boffin et al. (2014) reported perturbations of the A-B orbital motions in the Luhman 16 system, suggesting the presence of a third body. Later, Sahlmann & Lazorenko (2015) using the same *Very Large Telescope (VLT)* data and those from the follow-up monitoring programme by Boffin et al., have excluded the presence of any third object with a mass greater than two Jupiter masses orbiting around either BD with a period between 20 and 300 d.

Past and present-day ground-based seeing-limited imaging- and adaptive-optics-facilities have fundamental limitations (field of view, PSF stability, differential atmospheric chromatic effects, seasonal visibility), all of which introduce systematic and seasonal astrometric errors that are difficult to quantify or isolate when constraining the presence of companions via astrometry. This is particularly true for faint and red objects, which are much redder than the stars used as reference in the field. In the case of Luhman 16, there is the additional complication of observing a tight binary system (at an average separation of $\sim 1''$ and down to $0.22''$, see next sections). In the past, these systematic errors have resulted in false detections of planetary companions. These include reports of exoplanets orbiting Lalande 21185 (van de Kamp & Lippincott 1951, Lippincott 1960) and Barnard's star (van de Kamp 1963, 1969), both later refuted (Gatewood & Eichhorn 1973, Gatewood 1974). More recently, a giant planet was claimed to orbit the M8 dwarf VB 10 by Pravdo & Shaklan (2009) based on ground-based astrometric observations, a claim subsequently refuted by Lazorenko et al. (2011), among others. These and other examples point to the importance of high-precision-sub-milliarcsecond (mas)-space-based astrometry for robust detection of exoplanets around very low-mass stars and BDs.

For these reasons, we have used the *Hubble Space Tele-*

scope (HST) in a special mode to obtain the most accurate annual parallax of any BD to date (eventually down to the 50 micro-arc second level, μ as) for each of the two components of Luhman 16, and to constrain their absolute space motions with similar accuracy. Most importantly, by searching for astrometric perturbation of the A-B orbital motion, we will be able to confirm whether giant planet candidates exist in this system uncovering exoplanets down to a few Earth-masses, as described below. Our *HST* data could also potentially complement/extend the work done by Melso et al. (2015) searching for giant planets as resolved, faint companions comoving with the targets; however, we will see that this is not the case.

In this first article, we focus on the standard imaging analysis of our existing *HST* data using procedures and methods widely used in literature, sufficient to significantly improve characterization of this brown-dwarf binary system. In Section 2 we detail our observing strategy. In Sect. 3 we describe our data reduction and measurements. We explore two methods to derive astrometric and orbital parameters, through simultaneous fit of the parameters (Section 4) and through a two-step fitting procedure (Section 5). In Section 6 we use the limited radial velocities for the two components available in the literature to remove the degeneracy in the sign of the orbital inclination. In Sect. 7 we examine the photometric variability of the sources. In Sec. 8 we examine the potential presence of exoplanets based on this analysis, ruling out the presence of planets more massive than one Neptune-mass, and pointing out several-mas level inconsistencies between *HST* and existing ground-based astrometry from Sahlmann & Lazorenko (2015, hereafter SL15). In Sect. 9, we summarize the electronic material released as part of this work. In Sect. 10 we summarize our conclusions.

2 OBSERVING STRATEGY

The imaging data acquired for this project are obtained with the *Ultraviolet-VISual (UVIS)* channel of the *Wide Field Camera 3 (WFC3)* instrument on *HST* under programs GO-13748 and GO-14330 (PI: Bedin). UVIS has a wide field of view of about 160×160 arcsec² and the best image-quality on-board of *HST*, with two detectors of $\sim 4,000 \times 2,000$ pixels², and a pixel scale of ~ 39.77 mas.

The main goal of our program is to probe Luhman 16 AB for the presence of additional, yet unknown bodies, down to ~ 5 Earth-masses, through astrometric perturbations of the A-B orbital motion. Our observations were designed to maximize the high-precision astrometric capabilities of the *HST* with the relatively new cutting-edge technique of spatial-scanning mode. Spatial scanning under Fine Guide Sensors (FGS) control is an observing mode implemented for WFC3 on *HST* only recently, with the original aim of high-precision photometry during exoplanet transits (McCullough & MacKenty 2012). In this mode the target field is observed while the telescope slews in a specified direction and rate. This spatial scanning enables up to thousands of times more sampling of the same sources (targets and references), boosting photometric precision over pointed imaging. In the following we will refer to these images in spatial-scanning mode as *trailed*, and to those obtained in the standard mode as *pointed*. Recently, Riess

et al. (2014) employed this newly developed *HST* observing mode for WFC3 also to the case of astrometry. By scanning perpendicularly to the long axis of the parallax ellipse, this mode can considerably improve the precision of parallax measurements. Riess et al. demonstrated the possibility to measure changes in a source’s position to a precision of 20–40 μas . This is almost an order of magnitude better than what is attainable employing the best techniques in traditional pointed imaging with the WFC3/UVIS (i.e., 320 μas , see Bellini, Anderson & Bedin, 2011). As a rule of thumb, the astrometric precision essentially scales with the length of the trails. As in point-source imaging all the weight comes from the innermost 5-pixels, therefore trailing for 2,000 pixels, results in a $2000/5 = 400$ times more pixels, and therefore the gain is a factor of $\sqrt{400} = 20$. Accurate calculations are more complicated, and residuals in geometric distortion, currently calibrated down to 320 μas (Bellini et al. 2011) need to be suppressed to make this potential gain usable down to 20 μas (Casertano et al. 2016). There are important differences between our observing mode and analyses, and those proposed by Riess et al. (2014) or Casertano et al. (2016), which will be discussed in a subsequent paper analysing the trailed images.

The data for this project are collected in 13 visits at well-defined epochs, 5 at the maximum elongations of the parallax, and 8 at fractional phases of the year at (approximate) logarithmic sampling. Sampling periods are between 30 days and 3 years. Twelve of these visits have been collected.

The images (two-dimensional data) collected in thirteen epochs provide 26 independent data points to solve for the Luhman 16 AB barycentric positions, barycenter motions, parallax, mass-ratio, and for the seven parameters of the A-B orbit (13 parameters), plus detection of any significant deviation. Naturally, *it would not be possible* to firmly constrain the A-B orbit until at least half of the orbit will be completed, but we would still be able to firmly detect deviations from a conic arc, induced by additional bodies, at least for periods between ~ 30 days up to ~ 3 years.

The roll angle (hereafter, PA_{V3} , i.e., the position angle of axis V3 of the *HST*’s focal plane¹) was varied among the visits to minimize hidden systematic errors. Data were acquired in 6 different roll-angle values, with each roll-angle used on at least two visits. The dither pattern within each epoch was also carefully designed. We imposed large dither-steps of at least ± 100 pixels to have a check on the distortion residuals. We also avoided having Luhman 16 A and B fall on any of the lithographic features or other known cosmetic defects of the two UVIS CCDs (see Bellini et al. 2011), or in the gap between the two chips. Two known extra-galactic sources also fell in all images, which will be used in future works as an external check on absolute positions.

The main astrometric trailed exposures are collected in filter WFC3/UVIS/F814W. Although a medium or narrow band filter would be better for astrometry, as PSFs would be less dependent on the color of the targets, filter F814W has the valuable property that both Luhman16A and B have almost the same count rates. Furthermore, the F814W fil-

ter has one of the best characterized geometric distortion solutions (Bellini, Anderson & Bedin 2011).

Future analyses of the trailed images require pointed images to characterize the sources in the patch of sky (targets and the reference stars) and color information to trace potential chromatic dependencies. Therefore, two 60 s short pointed exposures in F814W are also taken at the beginning and at the end of each orbit to provide an input list, where both components of Luhman 16 are just below saturation level, i.e., at the maximum astrometric S/N possible. Next, to get the color information of the sources in the field, we choose the filter WFC3/UVIS/F606W, which is sufficiently bluer than F814W, and the best compromise between depth and reasonable signal for the cool components of Luhman 16. Due to the time required by the frame buffer dump, the exposure time for an optimal duty cycle is ~ 350 s. Our trailed exposures have at least this exposure times, and when visibility allows it, even longer. Therefore, in addition to the two short exposures, we could not fit more than five long exposures per orbit, of which four are trailed in F814W, and one is a pointed image in F606W. Seven exposures per orbits means that in the end there will be 52 trailed images of at least 350s in F814W, and 39 pointed images, 26 of which of 60 s in F814W and 13 of ~ 350 s in F606W, for a grand total of 91 images. So far 12 of 13 visits have been collected, i.e., 36 pointed images are available.

This article is based —exclusively— on these pointed images, 24 in filter F814W and 12 in filter F606W. Table 1 gives information on these 36 images.

3 DATA REDUCTIONS AND MEASUREMENTS

In this section we provide a brief description on how the positions in pixel coordinates (x, y) for all the stars in the individual frames were obtained, transformed into a common reference frame (X, Y) , and into a standard equatorial coordinate system (α, δ) at Equinox J2000. At each step we also give reference to works containing more exhaustive descriptions of the adopted procedures and software.

3.1 Correction for imperfect CTE

Imperfections in the charge transfer efficiency (CTE) smear the images, which result in compromised astrometry (see Anderson & Bedin 2010). In all our observations we have mitigated the CTE effects in two ways: (1) *passive CTE-mitigation*: we have downloaded the `_f1c` images, which apply the pixel-based CTE correction algorithms developed for the *Wide Field Channel* (WFC) of the *Advanced Camera for Surveys* (ACS) (Anderson & Bedin 2010) and are already implemented also for WFC3/UVIS images by the STScI pipeline. They are now downloadable as standard data-products at the MAST archive.² (2) *active CTE-mitigation*: We have applied a post-flashing (of about $12 e^-$) to keep the background above the critical threshold (filling many of

² The Mikulski Archive for Space Telescopes (MAST) is a NASA funded project. MAST is located at the Space Telescope Science Institute (STScI). <http://archive.stsci.edu/hst>

¹ WFC3 Instrument Handbook Chapter 2.2, Dressel et al. 2017.

Table 1. *HST* images used in this work (ID is not in MJD order).

#ID: MJD _{start}	image	EXPT	PA _{V3} [°]
F814W			
01: 56891.03123284	icmw09v1q	60 s	345.010712
02: 56891.10048062	icmw09waq	60 s	345.006592
03: 56935.09556248	icmw0411q	60 s	40.016430
04: 56935.12740285	icmw041cq	60 s	40.013191
05: 57031.75281042	icmw02z1q	60 s	144.999603
06: 57031.82073857	icmw02zwq	60 s	145.003006
07: 57059.93495262	icmw12asq	60 s	160.003403
08: 57059.96679262	icmw12b3q	60 s	160.007401
09: 57115.70210654	icmw07ccq	60 s	215.013794
10: 57115.73394691	icmw07cnq	60 s	215.017197
11: 57204.00903025	icmw01vbq	60 s	325.005707
12: 57204.07274544	icmw01vyq	60 s	325.002289
13: 57255.02930926	icmw10bsq	60 s	345.010712
14: 57255.06114963	icmw10caq	60 s	345.006592
15: 57300.55774736	icmw05dfq	60 s	40.016430
16: 57300.59198366	icmw05dqq	60 s	40.013191
17: 57395.65852572	icmw03xoq	60 s	144.999603
18: 57395.69036609	icmw03xzzq	60 s	145.003006
19: 57429.21396601	icmw13uyq	60 s	161.070297
20: 57429.28672083	icmw13v9q	60 s	161.074203
21: 57479.56281007	icmw08bvq	60 s	215.013794
22: 57479.62306489	icmw08c6q	60 s	215.017197
23: 57665.08973572	icmw06rvq	60 s	40.016430
24: 57665.12157609	icmw06saq	60 s	40.013191
F606W			
25: 56891.04534173	icmw09v8q	348 s	345.008606
26: 56935.10967137	icmw0416q	348 s	40.014809
27: 57031.76691931	icmw02zqq	348 s	145.001297
28: 57059.94906114	icmw12axq	348 s	160.005402
29: 57115.71621543	icmw07chq	348 s	215.015503
30: 57204.02463210	icmw01vhq	348 s	325.003998
31: 57255.04341815	icmw10c2q	348 s	345.008606
32: 57300.57305995	icmw05dkq	348 s	40.014809
33: 57395.67263424	icmw03xtq	348 s	145.001297
34: 57429.25623453	icmw13v3q	348 s	161.072296
35: 57479.57691896	icmw08c0q	348 s	215.015503
36: 57665.10384461	icmw06s3q	348 s	40.014809

the charge-traps), which suppress as much as convenient the residuals due to imperfect CTE.³ However, both strategies do not work perfectly, and traces of these imperfect CTE remain. The residuals left on the measured positions are sizable (~ 0.5 mas), but thankfully, they are also (relatively) easy to track down and remove (see following Sections).

3.2 Fluxes and positions in the individual images

Positions and fluxes of sources in each WFC3/UVIS `_f1c` image were obtained with software that is adapted from the program `img2xym_WFC.09x10` developed for ACS/WFC (Anderson & King 2006), and publicly available.⁴ Together with

the software, a library of *effective* PSFs for most common filters is also released. These are spatially variable in a 7×8 array, and can also be perturbed in a spatially constant mode to better fit PSFs of individual frames. However, we follow the Bellini et al. (2013) prescription to perturb the library PSFs also spatially (in a 5×5 spatial array). These procedures tailor the library PSFs to each individual image even better than spatially-constant perturbed PSFs, as they better account for small focus variations across the whole field of view. In addition to solving for positions and fluxes, the software also provides a quality-of-fit parameter (Q). The quality-of-fit essentially tells how well the flux distribution resembles the shape of the point spread function (this parameter is defined in Anderson et al. 2008). It is close to zero for stars measured best. This parameter is useful for eliminating galaxies, blends, and stars compromised by detector cosmetic or artifacts.

Once the raw pixel positions ($x^{\text{raw}}, y^{\text{raw}}$) and magnitude are obtained, they are corrected for geometric distortion. We used the best available average distortion corrections for WFC3/UVIS (Bellini & Bedin 2009; Bellini, Anderson & Bedin 2011) to correct the raw positions and fluxes of sources that we had measured within each individual image. (Note that fluxes are also corrected for pixel area using the geometric distortion correction). We refer to corrected positions in the individual frame with the symbols ($x^{\text{cor}}, y^{\text{cor}}$).

Finally, we note that given the large width of the filter pass-band of F606W and F814W, the PSFs for very red stars are significantly different from the PSFs of average-color stars in the field. This fact is evident in the relatively large values of Q for Luhman 16 A and B, compared to stars of similar magnitudes; and residuals in the subtracted images of Luhman 16 A and B. These fit mismatches could potentially lead to chromatic systematic errors in positions, known to affect UV filters (Bellini et al. 2011). However, as described below, such offsets are below the level of other systematic errors (i.e., $\sim 320 \mu\text{s}$ for geometric distortion) for this analysis.

3.3 The reference frame

As our *reference frame* we adopted the best-fit (~ 200) stars measured in the first exposure of our first epoch. These stars were unsaturated, with at least $4,000 e^-$, isolated by at least 9 pixels, and with $Q < 0.4$. To avoid negative values when stacking all images from all epochs (see next section), we added 1000.0 pixels in each coordinate to the distortion-corrected positions of these stars; the resulting coordinates are indicated with (X, Y) and are the positions in our adopted reference frame. We then find the most general linear transformation (6-parameters), between the distortion-corrected positions of these stars of the reference-frame (X, Y), and their distortion-corrected positions ($x^{\text{cor}}, y^{\text{cor}}$) in any other image (for as many stars in common as possible). This enables us to perform all of the relative measurements with respect to this reference frame. These transformations were computed using only stars with positions consistent to at least 3.6 mas (or 0.09 pixels). This ensured that we use only stars that are present in all imaging epochs and do not have compromised measurements due to cosmic rays or detector cosmetics. The underlying assumption is that stars in the field have negligible common and peculiar

³ http://www.stsci.edu/hst/wfc3/ins_performance/CTE/

⁴ <http://www.stsci.edu/~jayander/WFC3/>

Table 2. Observed positions for Luhman 16 A and B in both the master frame coordinate system and in the raw coordinate system of the individual images. The ID is as in Table 1.

#ID	X_A^{obs}	Y_A^{obs}	x_A^{raw}	y_A^{raw}	X_B^{obs}	Y_B^{obs}	x_B^{raw}	y_B^{raw}
01	3177.4275	4480.9977	2180.594	3248.659	3200.5454	4483.9296	2203.846	3249.985
02	3177.4303	4481.0021	2382.559	3031.726	3200.5414	4483.9315	2405.762	3033.062
03	3176.9366	4479.5016	2884.488	2699.714	3198.7634	4481.8825	2898.892	2682.114
04	3176.9435	4479.5022	3084.968	2484.191	3198.7643	4481.8713	3099.326	2466.629
05	3184.4565	4459.9769	2196.945	1018.424	3203.3583	4461.0975	2179.580	1012.017
06	3184.4761	4459.9582	2397.461	805.277	3203.3756	4461.0672	2380.121	798.883
07	3192.5751	4453.7701	1675.234	1020.767	3210.5832	4454.5311	1657.325	1019.570
08	3192.5676	4453.7692	1876.887	807.325	3210.5920	4454.5209	1858.992	806.127
09	3214.1073	4447.1471	978.149	1568.796	3230.3335	4447.1769	967.574	1581.945
10	3214.1009	4447.1548	1181.296	1353.836	3230.3353	4447.1909	1170.739	1366.957
11	3242.2848	4452.4870	1717.135	3241.691	3255.6215	4451.3658	1730.160	3244.327
12	3242.3069	4452.4778	1920.016	3024.247	3255.6413	4451.3684	1933.013	3026.896
13	3247.3853	4456.4204	2247.516	3213.591	3258.9968	4454.6607	2259.184	3210.991
14	3247.3841	4456.4230	2449.420	2996.722	3259.0010	4454.6512	2461.070	2994.122
15	3247.0263	4454.9574	2900.188	2632.622	3257.0703	4452.6038	2903.983	2622.733
16	3247.0203	4454.9533	3100.615	2417.148	3257.0684	4452.5891	3104.392	2407.270
17	3254.4639	4435.7435	2131.405	1031.633	3261.1672	4432.1937	2123.896	1033.147
18	3254.4433	4435.7412	2332.359	818.548	3261.1601	4432.1852	2324.849	820.057
19	3264.2778	4428.4527	1594.860	1046.116	3269.8193	4424.4668	1589.037	1050.078
20	3264.3006	4428.4303	1796.647	832.784	3269.8390	4424.4459	1790.841	836.733
21	3283.9823	4422.6438	939.376	1641.428	3287.7122	4418.0588	940.481	1647.189
22	3283.9962	4422.6308	1142.653	1426.469	3287.7264	4418.0350	1143.768	1432.227
23	3317.6832	4430.3163	2920.286	2558.888	3314.7398	4423.5832	2913.082	2557.926
24	3317.6947	4430.3326	3120.572	2343.566	3314.7544	4423.5828	3113.368	2342.590
25	3177.4460	4481.0101	2281.575	3139.634	3200.5467	4483.9358	2304.789	3140.960
26	3176.9415	4479.5348	2984.632	2591.444	3198.7467	4481.9008	2998.996	2573.871
27	3184.4592	4459.9705	2297.332	911.318	3203.3471	4461.0937	2279.990	904.925
28	3192.5569	4453.7925	1776.067	913.452	3210.5696	4454.5195	1758.167	912.284
29	3214.1096	4447.1664	1079.659	1460.824	3230.3390	4447.1832	1069.104	1473.969
30	3242.3159	4452.4941	1818.561	3132.291	3255.6412	4451.3722	1831.562	3134.924
31	3247.3933	4456.4421	2348.386	3104.735	3259.0001	4454.6511	2360.038	3102.110
32	3247.0193	4454.9672	3000.366	2524.365	3257.0534	4452.6149	3004.151	2514.496
33	3254.4318	4435.7819	2231.914	924.491	3261.1580	4432.2029	2224.381	926.023
34	3264.3046	4428.4673	1695.718	938.990	3269.8228	4424.4705	1689.925	942.958
35	3283.9613	4422.6474	1041.177	1533.354	3287.6950	4418.0489	1042.291	1539.121
36	3317.6784	4430.3462	3020.289	2450.742	3314.7539	4423.6158	3013.104	2449.764

motions; however an uncertainty of 3.6 mas on ~ 200 stars still leads to an uncertainty of $250 \mu\text{as}$ on the centroid position. In this work we will not attempt to iteratively solve for the motions of individual reference field objects, as again, these uncertainties are of the same order of the precision of the astrometry in pointed images. We will see in Sect. 3.4 how this positional precision is consistent with *Gaia* DR1 positions.

For the same reasons, and differently from the more sophisticated local-transformations procedure described in Bedin et al. (2014), we do not apply any local approach, due to the relatively low stellar density in the field, and as our final residuals using global transformations are already consistent with our expected uncertainties.

The observed positions in the (X, Y) reference frame for Luhman 16 A and B in the 36 pointed images analyzed in this work are given in Table 2. There, we also give the $(x^{\text{raw}}, y^{\text{raw}})$ positions which will be used to track down the

systematic effects of residuals of imperfect CTEs, and to correct for them.

3.4 Absolute Astrometric Calibration

We anchor our reference frame to the astrometric system of the *Gaia* first data-release (DR1, The *Gaia* collaboration, 2016), which is tied to the ICRS for equinox J2000.0, and at epoch 2015.0.

As extensively discussed in Bedin et al. (2014), any adopted geometric distortion correction for *HST* cameras is just an average solution, as from frame to frame there are sizeable changes, mainly induced by velocity aberration (Cox & Gilliland 2003) and focus variations (the so called *breathing* of the telescope tube as a result of different incidence of light from the Sun). This is particularly true for the linear terms of the distortion, which contain the largest portion of these changes. We used six-parameter linear transformations to register the distortion-corrected positions measured in each

Table 3. Adopted coefficients to transform the observed tangential plane coordinates of the reference frame $(2X, 2Y)$ into equatorial coordinates of Gaia DR1 equinox J2000.0, at epoch 2015.0 (α, δ) , which are linked to the ICRS.

\mathcal{A}	$(-4.79474 \pm 0.00025)E - 06$
\mathcal{B}	$(+2.74144 \pm 0.00025)E - 06$
\mathcal{C}	$(+2.74145 \pm 0.00025)E - 06$
\mathcal{D}	$(+4.79468 \pm 0.00025)E - 06$
X_0	$+6062.888 \pm 0.004$
Y_0	$+6832.005 \pm 0.004$
α_0	162.302050 (defined)
δ_0	-53.328911 (defined)

frame $(x^{\text{cor}}, y^{\text{cor}})$ to the distortion-corrected positions of the reference frame (X, Y) . The linear-term variations with respect to the reference frame are almost completely absorbed by these six-parameter linear transformations. However, the linear terms of the reference frame remain to be determined: astrometric zero-points, plate scales, orientations, and skew terms need to be calibrated to an absolute reference system. To avoid under-sampling in our stacked image we derive the transformation from *Gaia* to our reference frame super-sampled by a factor of 2, hereafter indicated as $(2X, 2Y)$, see next section.

Within our Luhman 16 AB WFC3/UVIS field of view we found 126 *Gaia* DR1 point sources in common with our reference frame which we used to calibrate our six linear terms. To do this, we assume our $(2X, 2Y)$ as a tangential plane in the tangent point (α_0, δ_0) , and matched the $(\alpha - \alpha_0, \delta - \delta_0)$ differences with our $(2X, 2Y)$. We then find the linear transformation between $(\alpha - \alpha_0, \delta - \delta_0)$ and $(2X, 2Y)$, by solving for the six parameters $\mathcal{A}, \mathcal{B}, \mathcal{C}, \mathcal{D}, X_0, Y_0$ in the system:

$$\begin{cases} \alpha^* = (\mathcal{A}(2X - X_0) + \mathcal{B}(2Y - Y_0)) + \alpha_0 \\ \delta = (\mathcal{C}(2X - X_0) + \mathcal{D}(2Y - Y_0)) + \delta_0 \end{cases}$$

Where $\alpha^* = \alpha \cos \delta$. All 126 stars in common with Gaia DR1 agree to within 40 mas with positions in $(2X, 2Y)$. Of the 67 within 1 mas, we noticed a bulk of very consistent stars. To derive the six coefficients we used only the 21 stars with consistent Gaia positions to within 0.6 mas. The coefficients of the transformations are given in Table 3.

The plate-scale derived from *Gaia* DR1 of our super-sampled reference frame $(2X, 2Y)$ is $\sqrt{|\mathcal{A}\mathcal{D} - \mathcal{B}\mathcal{C}|} = 19.883$ mas, meaning that the assumed pixel scale of (X, Y) is 39.766 mas. This is in good agreement with values of the WFC3/UVIS pixel scale independently derived by Bellini et al. (2011).

The non-linear part of the WFC3/UVIS distortion solutions should be accurate to much less than 0.01 original-size WFC3/UVIS pixel (~ 0.3 mas in a global sense, Bellini et al. 2011), roughly the random positioning accuracy with which we can measure a bright star in a single exposure. Note that the linear terms of the ACS/WFC distortion solution have been changing slowly over time (Anderson et al. 2007; Ubeda, Kozurina & Bedin 2013). Even if this is the case for WFC3/UVIS, having linked our linear terms to the *Gaia* DR1 makes our astrometric solution immune to those effects, as well as to those of velocity aberration, breathing, etc. Therefore our absolute coordinates are referred to the

ICRS *Gaia* DR1 in equinox J2000.0, with positions given at the reference epoch, 2015.0 (The *Gaia* collaboration, 2016).

3.5 Image stack

Having at hand all the transformations from the coordinates of each image into the reference frame, it becomes possible to create a stacked image of the field for each epoch, and a sum of these stacks. The stack provides a representation of the astronomical scene that enables us to independently check the region around each source at each epoch. The stacked images are $13\,000 \times 13\,000$ pixels² in the $(2X, 2Y)$ reference system, i.e., super-sampled by a factor of two (~ 20 mas pixel⁻¹). The image sum of the stacks for the 12 epochs is shown in Fig. 1. We have included in the header of the image (in the form of World Coordinate System keywords) our absolute astrometric solution, which is based on the *Gaia* DR1 source catalog, as described in the previous section. As part of the electronic material provided in this paper, we also release the stacked average image, and the sum of the stacked images for all epochs in F814W; all with our astrometric solution in the header in the form of World Coordinate System (WCS).

In the next two sections we will describe the determination of the astrometric and orbital parameters of the Luh 16 AB system employing two different methods.

4 METHOD A: SIMULTANEOUS DETERMINATION OF ASTROMETRIC AND ORBITAL PARAMETERS

Our reference system is not an absolute reference frame, as even the stars that moved the least and with the most robust positions are not at an infinite distance. On the basis of a Besançon Galactic model (Robin et al. 2004), we expect that our best measured stars used to define the (X, Y) reference frame lie at an average distance of ~ 5 kpc. This would introduce a correction from relative to absolute of about 0.2 mas to our parallax and motions.

As noted previously, in this first analysis we aim for an accuracy equivalent to geometric distortion, about 0.3 mas. Hence, to first approximation we assume our measured positions are on an absolute system. Rather than fitting the relative orbit (seven parameters) and the absolute motion of the barycenter plus the mass ratio (six parameters) separately, a thirteen-parameter model of the independent motions of Luhman 16 A and B is adopted. In terms of complexity, the computational cost of fitting both models is the same; however, fitting a model looking at the separate component motions makes it possible to measure the correlation between any pair of the thirteen parameters, and thus deviation from that model for a planet orbiting one of the components.

The positions $(\alpha^* = \alpha \cos \delta, \delta)$ of the two components (k) can be expressed as

$$\begin{cases} \alpha_1^* = \alpha_0^* + \varpi f_a + \mu_{\alpha^*} \Delta t + B X(t) + G Y(t) \\ \delta_1 = \delta_0 + \varpi f_d + \mu_{\delta} \Delta t + A X(t) + F Y(t) \\ \alpha_2^* = \alpha_0^* + \varpi f_a + \mu_{\alpha^*} \Delta t - B \rho X(t) - G \rho Y(t) \\ \delta_2 = \delta_0 + \varpi f_d + \mu_{\delta} \Delta t - A \rho X(t) - F \rho Y(t) \end{cases} \quad (1)$$

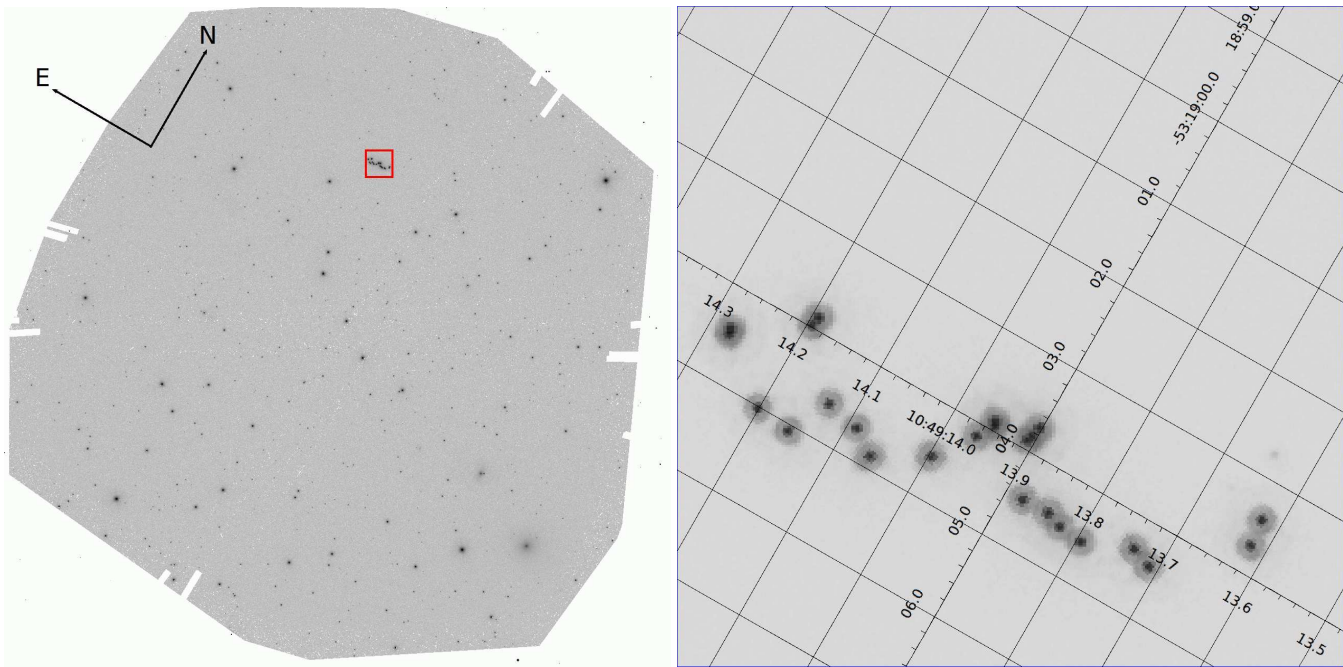


Figure 1. (Left:) The region surrounding Luhman 16 AB, as monitored by *HST*. It has dimensions of about $160'' \times 160''$ and is the sum of the stacks in WFC3/UVIS/F814W obtained for each of the 12 individual visits considered in this work. (Right:) Zoom-in of the same image in the portion highlighted by a red square. It has a size of $7'' \times 7''$ and shows the complete pattern in the sky of Luhman 16 A and B during the period monitored by our *HST* observations. The orientation is the one of the master frame, while a fine grid ($1''$) gives equatorial coordinates.

where (α_0^*, δ_0) are the position of the baricenter of the system at the reference epoch (here 2015.0). f_a and f_d denote the parallactic factors (van de Kamp 1967), ϖ the parallax, and μ the proper motions along α^* and δ . For the sake of linearity, we adopt the Thiele-Innes formalism of the orbital contribution:

$$X(t) = \cos E - e \quad (2)$$

$$Y(t) = \sqrt{1 - e^2} \sin E \quad (3)$$

$$E = \frac{2\pi}{P}(t - T_0) + e \sin E \quad (4)$$

$$A = a_1(\cos \omega \cos \Omega - \sin \omega \sin \Omega \cos i) \quad (5)$$

$$B = a_1(\cos \omega \sin \Omega + \sin \omega \cos \Omega \cos i) \quad (6)$$

$$F = a_1(-\sin \omega \cos \Omega - \cos \omega \sin \Omega \cos i) \quad (7)$$

$$G = a_1(-\sin \omega \sin \Omega + \cos \omega \cos \Omega \cos i) \quad (8)$$

where a_1 is the angular semi-major axis of the absolute orbit of the primary component, ω is the argument of the periastron of the primary, Ω is the longitude of the node, i is the inclination of the orbital plane with respect to the plane orthogonal to the line of sight, e is the eccentricity of the orbit, P the orbital period and T_0 one epoch of periastron passage.

Assuming that model, the parameters which minimize the sum of the residuals squared (for both components, both in α^* and δ) are adopted as the solution. Owing to the nature of the model (motion of the baricenter and orbit of both components), the gradient of that sum is nonlinear and one therefore needs a reliable initial guess of the solution before calling any local minimization method (e.g., Levenberg-Marquardt, Marquardt 1963). Even if our model is globally nonlinear, the minimization problem can be reorganized as

two nested ones, the inner one containing all the parameters that appear linearly in the gradient of the original sum. If $F(p_1, \dots, p_{13})$ denotes that sum with p_k ($k = 1 \dots 13$) the different parameters, one can rewrite the minimization of F as

$$\min_{(p_1, \dots, p_{13})} F(p_1, \dots, p_{13}) = \quad (9)$$

$$= \min_{(p_{10}, \dots, p_{13})} \min_{(p_1, \dots, p_9)} F(p_1, \dots, p_9, \underline{p_{10}}, \underline{p_{11}}, \underline{p_{12}}, \underline{p_{13}}) \quad (10)$$

where, for the sake of simplicity, it is assumed that the last four parameters are those that appear non-linearly in the model (namely the eccentricity, the orbital period, an epoch of periastron time, and the scaling factor ρ). The notation $\underline{p_k}$ means that p_k remains unchanged.

In these nested minimizations, the inner one is linear and thus takes no iteration to reach the minimum. Therefore, one ends up with a simpler nonlinear model with four parameters only. An initial guess of that 4-dimensional nonlinear problem can be obtained through a basic grid search before the whole 13-parameter nonlinear objective function is minimized with, say, Levenberg-Marquardt.

The residuals of this model exhibit a seasonal variation along both axes (α^* and δ) for both components. The periodicity (one year) and the fact that this variation is present in every residual rule out the presence of a companion as an explanation. If, instead of these natural residuals versus time, one plots the residuals in X and Y versus x_{raw} and y_{raw} , the seasonal variation becomes a straight line, thus revealing the presence of some CTE residual in the observations. Four straight lines are adjusted to correct for CTE: one for each axis and each filter. [Note that at each of the 13 epochs we have 3 observations in

Table 4. Astrometric and orbital parameters of Luhman 16 AB obtained with a simultaneous fit described in Sect. 4. The coordinates are in J2000.0, epoch 2015.0.

α^* (deg.) ^a	+96.9342078	$\pm 7.68\text{E}-07$
δ (deg.)	-53.3179180	$\pm 5.06\text{E}-07$
ϖ (mas)	501.14	± 0.052
μ_{α^*} (mas/yr)	-2763	± 1.45
μ_{δ} (mas/yr)	+358	± 1.75
A (mas)	+530	± 58.8
B (mas)	-410	± 348
F (mas)	+49	± 1490
G (mas)	-183	± 1250
e	0.25	± 0.0648
P (yr)	19	± 20.2
T_0 (Jul.yr)	2000	± 24.6
ρ	+1.22	± 0.0214

^a $\alpha^* = \alpha \cos \delta$.

two coordinates, so 72 independent data points, for twelve epochs.] Once the CTE residuals are corrected for, a new model fit is carried out. The thirteen parameters resulting from that minimization are listed in Table 4. The typical residual is 0.39 mas.

Despite the exquisite precision of the *HST* data, there are difficulties in obtaining a reliable simultaneous fit of the astrometric and orbital parameters using only a partial arc of the orbit. It is particularly unsatisfactory that the orbital period that results is largely unconstrained (see Table 4), and so too the individual masses. Similar difficulties to obtain a simultaneous fit were reported previously by Sahlman & Lazorenko (2015, Sect. 3.1), who used an even shorter orbital arc than ours. Among other inconsistencies in their simultaneous solutions, they noted a strong anti-correlation between the residuals for the A and B components much larger than their measurement uncertainties, indicating that the motion of A and B were not independent and should be modelled globally. We therefore analyzed our own A and B motion residuals, and found that the Pearson correlation coefficients are ~ 0.65 for both the α^* and δ components of our solution, indeed indicating a degree of correlation much larger than our expected uncertainties.

It is not clear how and why the accuracy of the simultaneous fit solution is degraded using a partial arc of the orbit. We suspect a complicated interplay with CTE residuals, field-targets color dependencies in the PSFs, or just the deviations from the absolute positions, all of which might propagate in the solution.

Therefore, until distances with *Gaia* for the reference field stars or data covering more of the orbital phase will be available, we now abandon the simultaneous fit of (absolute) astrometric and orbital parameters, and explore in the next section a simpler and more robust (relative) approach.

5 METHOD B: TWO-STEP DETERMINATION OF ASTROMETRIC AND ORBITAL PARAMETERS

In a two-body system, at any time, the baricenter (indicated hereafter with G) lies along the segment connecting the two

components of the system, and the position of G along this segment is fixed by just one parameter, the mass ratio (hereafter, q).

In this second approach we obtain our solution in two steps. In the first step we determine q and the astrometric parameters of G (positions, proper motions and parallax), and in the second step we solve for the relative orbit, now using just the Luh16 A and B relative positions. Note that the derived astrometric parameters will be in the relative astrometric system of the reference frame ($2X, 2Y$), which is not an absolute system. The orbital solutions will not be affected by CTE residuals, because when looking at differences between A and B positions the effects of CTE should cancel-out at a great level of accuracy. The same is true for the PSFs' color-dependencies, as Luh 16 A and B have essentially the same color and they would be affected by the same systematic errors.

5.1 Step 1: Determination of Positions, Parallax, Proper Motions, and Mass-Ratio

In Fig. 1 we can see in one shot all the projected space motions during the first 12 epochs of our *HST* campaign in the period between August 22 2014 and October 4 2016, for both Luhman 16 A and B. Not all of the components in all the epochs are clearly distinguishable in this stacked image. More clear is Fig. 2 where we show the complete series of observed positions on the same reference frame ($2X, 2Y$) of Fig. 1, indicating Luhman 16 A with a filled dot, and B with an open circle. To better identify the epoch-pair, we connect the AB components with a black segment. Note that at each given epoch (i.e., one single-orbit *HST* visit) there are actually three dithered individual observations taken less than an hour apart, which we can safely consider collected at the same astrometric epoch.

From the observed 36 2D-data points we would like to derive the baricenter of the Luhman 16 AB system (G) five astrometric parameters: its positions (X_G, Y_G), its motions (μ_{X_G}, μ_{Y_G}), and most importantly the system parallax π . However, the baricenter G is not an observable, but needs to be inferred from the relative positions of A and B components along their mutual orbit. So, we need to add to the unknown parameters the mass ratio q defined as $\mathcal{M}_B/\mathcal{M}_A$ (i.e., $0 < q < 1$, where \mathcal{M} indicate the mass of each component). In the following we will describe the procedure followed to fit these six parameters.

By virtue of the principle that any transformation of the observational data degrades them, while numerical models do not, we perform this numerical fitting process directly in the observational plane ($2X, 2Y$). To accomplish our fit, we proceed iteratively solving for the best fit of the data, then de-trending for CTE residuals, and finally fitting again the CTE-de-trended data.

To predict the position of the baricenter we make use of the sophisticated tool by U.S. Naval Observatory, the *Naval Observatory Vector Astrometry Software*, hereafter NOVAS⁵ (in version F3.1, Kaplan et al. 2011), which accounts for many subtle effects, such as the accurate Earth

⁵ http://aa.usno.navy.mil/software/novas/novas_f/-novasf_intro.php

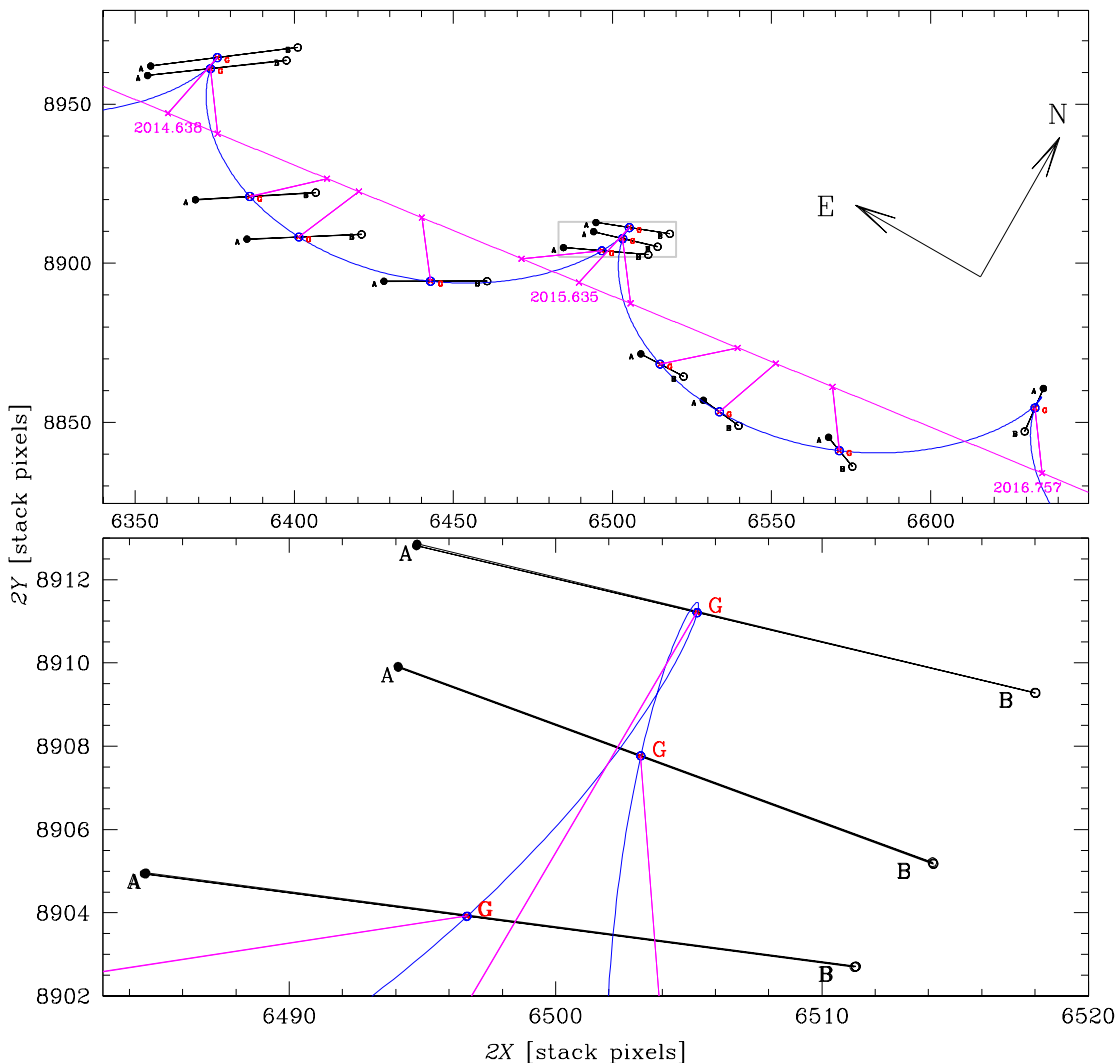


Figure 2. The top panel shows the complete series of observed positions for Luhman 16 A (filled circles) and Luhman 16 B (empty circles) in the coordinate system of our master frame. At any given epoch a black line join A and B, and along it is marked with a red cross the position of the baricenter, G, estimated as explained in the text. A blue curve indicate the astrometric solution for the Luhman 16 AB’s baricenter (positions, proper motions, parallax), noting that the mass ratio, q , (i.e., the baricenter itself) is part of the solution. A line in magenta indicate the same solution with the system at an infinite distance, and crosses in magenta on this line indicate the individual epochs on this. These locations are connected with the observed baricentric positions. The orientations in this plot are the same of the master frame, as in Fig. 1. The bottom panel shows details for these curves around epoch 2015.6, in a region indicated in the top panel with a gray rectangle; this panel shows how finely observations were reproduced.

orbit, perturbations of major bodies, nutation of the Moon–Earth system, etc. We are not interested in the absolute astrometric calculations of NOVAS but only in the relative effects. In computing the positions we used an auxiliary star with no motion and zero parallax (i.e., at infinite distance), and finally compute the difference with respect to our targets. We then use a Levenberg–Marquardt algorithm (the FORTRAN version `lmdif` available under MINIPACK, Moré et al. 1980) to find the minimization of six parameters: $X_G, Y_G, \mu_{X_G}, \mu_{Y_G}, \pi$, and q .

The first iteration produced a solution with residuals as large as 2 mas, which were significantly larger than our expected errors, and most importantly clearly and simply

correlated with the x^{raw} and y^{raw} coordinates. We ascribed these residual mainly to CTE, but potentially also to differential chromatic and PSFs residuals correlated with roll-angles. The best fit is shown with a blue line in Fig. 2. A simple fit to the residuals of the Observed–Calculated (O–C) of baricenter $2X$ and $2Y$ as function of x^{raw} and y^{raw} deliver a correction that can be applied to the (X, Y) positions. We refer to these de-trended positions for both A and B components with the symbols $(X^{\text{dtr}}, Y^{\text{dtr}})$, which are given in Table 5. After this correction the (O–C) residuals are perfectly consistent with those expected for stars of this luminosity for WFC3/UVIS, i.e., 0.008 pixels, or, 320 μmas . Therefore we impute these remaining residuals to just random errors.

Table 5. De-trended coordinates for Luhman 16 A and B, with magnitudes and quality fit parameter.

#ID	X_A^{dtr}	Y_A^{dtr}	Q_A	mag _A	X_B^{dtr}	Y_B^{dtr}	Q_B	mag _B
01	3177.4290	4480.9726	.0595	-13.7789	3200.5478	4483.9043	.0678	-13.7686
02	3177.4385	4480.9813	.0554	-13.7958	3200.5502	4483.9105	.0712	-13.7514
03	3176.9600	4479.4869	.0706	-13.7721	3198.7869	4481.8681	.0822	-13.7836
04	3176.9733	4479.4917	.0642	-13.7539	3198.7938	4481.8611	.0747	-13.7483
05	3184.4585	4459.9941	.0569	-13.7644	3203.3598	4461.1151	.0758	-13.7225
06	3184.4847	4459.9796	.0662	-13.7687	3203.3837	4461.0890	.0822	-13.5614
07	3192.5618	4453.7872	.0606	-13.7936	3210.5695	4454.5485	.0789	-13.7416
08	3192.5604	4453.7906	.0657	-13.7925	3210.5842	4454.5426	.0714	-13.7596
09	3214.0726	4447.1540	.0486	-13.7717	3230.2991	4447.1838	.0573	-13.8035
10	3214.0726	4447.1658	.0520	-13.7789	3230.3068	4447.2018	.0745	-13.7369
11	3242.2729	4452.4620	.0560	-13.7351	3255.6101	4451.3406	.0756	-13.7226
12	3242.3008	4452.4571	.0636	-13.7869	3255.6356	4451.3474	.0668	-13.7521
13	3247.3892	4456.3960	.0562	-13.7746	3259.0011	4454.6361	.0623	-13.7179
14	3247.3943	4456.4028	.0615	-13.7785	3259.0115	4454.6309	.0709	-13.7319
15	3247.0500	4454.9440	.0645	-13.7750	3257.0941	4452.5905	.0723	-13.8075
16	3247.0505	4454.9441	.0696	-13.7775	3257.0982	4452.5800	.0804	-13.7487
17	3254.4639	4435.7605	.0700	-13.7896	3261.1670	4432.2108	.0666	-13.7592
18	3254.4500	4435.7624	.0735	-13.7754	3261.1665	4432.2065	.0804	-13.7109
19	3264.2620	4428.4694	.0685	-13.8066	3269.8034	4424.4836	.0635	-13.8043
20	3264.2910	4428.4512	.0777	-13.7803	3269.8294	4424.4669	.0838	-13.7612
21	3283.9466	4422.6495	.0872	-13.8059	3287.6769	4418.0644	.0925	-13.7280
22	3283.9666	4422.6405	.0800	-13.8129	3287.6971	4418.0447	.0858	-13.7983
23	3317.7075	4430.3043	.0729	-13.8042	3314.7639	4423.5710	.0730	-13.7451
24	3317.7254	4430.3247	.0736	-13.7757	3314.7844	4423.5749	.0851	-13.7410
25	3177.4511	4480.9871	.0438	-12.5274	3200.5524	4483.9125	.0326	-11.8824
26	3176.9679	4479.5222	.0549	-12.4756	3198.7734	4481.8883	.0542	-11.8233
27	3184.4647	4459.9898	.0608	-12.5185	3203.3521	4461.1134	.0353	-11.8406
28	3192.5469	4453.8118	.0426	-12.5346	3210.5591	4454.5391	.0418	-11.8384
29	3214.0780	4447.1755	.0514	-12.5449	3230.3074	4447.1921	.0474	-11.8699
30	3242.3070	4452.4713	.0514	-12.4980	3255.6328	4451.3491	.0495	-11.8312
31	3247.4004	4456.4198	.0377	-12.5136	3259.0075	4454.6286	.0336	-11.7717
32	3247.0462	4454.9560	.0514	-12.5031	3257.0802	4452.6036	.0472	-11.8295
33	3254.4352	4435.8009	.0692	-12.5472	3261.1611	4432.2221	.0551	-11.8479
34	3264.2919	4428.4862	.0422	-12.5278	3269.8101	4424.4895	.0492	-11.8609
35	3283.9286	4422.6551	.0405	-12.5847	3287.6626	4418.0566	.0542	-11.8742
36	3317.7059	4430.3364	.0445	-12.4950	3314.7809	4423.6060	.0438	-11.8031

Table 6. Astrometric parameters and mass-ratio of Luhman 16 AB.

$q = \mathcal{M}_B/\mathcal{M}_A$	0.848	± 0.023
$\alpha_{J2000.0}$ [hours]	10.82187776	± 65 mas
$\delta_{J2000.0}$ [degrees]	-53.3193958	± 45 mas
$\mu_{\alpha \cos \delta_{J2000.0}}$ [mas yr ⁻¹]	-2762.2	± 2.3
$\mu_{\delta_{J2000.0}}$ [mas yr ⁻¹]	354.5	± 2.8
π [mas]	501.118	± 0.093
$\varpi = \pi + 0.28 \pm 0.01$ [mas]	501.398	$\pm 0.093 \pm 0.01$

Our final astrometric solution is given in Table 6. To assess uncertainties we conservatively used the method of residual permutation, and take the 68-th percentile of the deviations from the mean as the 1- σ error. The relative parallax (which we indicate with π) is with respect to the most distant objects in the field (i.e., those that moved the least) and therefore π is only a lower limit to the absolute parallax ϖ . In a first approximation we can use the relative-to-absolute correction, which was derived by SL15

as 0.28 ± 0.01 mas. In Table 6 we also give the value derived for ϖ employing this correction. However, we note that our relative parallax, $\pi = 501.118 \pm 0.093$ mas, is already *significantly* larger than the absolute parallax by SL15, which is $\varpi = 500.51 \pm 0.11$ mas, therefore implying a closer distance for Luh 16 AB, at no more than 1.9955 ± 0.0004 pc. When *Gaia* parallaxes for reference stars will become available we will be able to determine an accurate relative-to-absolute correction for our π value.

5.2 Step 2: Determination of the Orbital Parameters

With q and the astrometric parameters of G derived in the previous step, the position of the barycenter is known at any given epoch. This enables us to plot in Fig. 3 the observed data points in equatorial coordinates relative to the barycenter, revealing that our data cover over 120° of the projected true anomaly along the orbits (i.e., $\sim 1/3$ of the projected orbit). We indicate the area swept during our observations

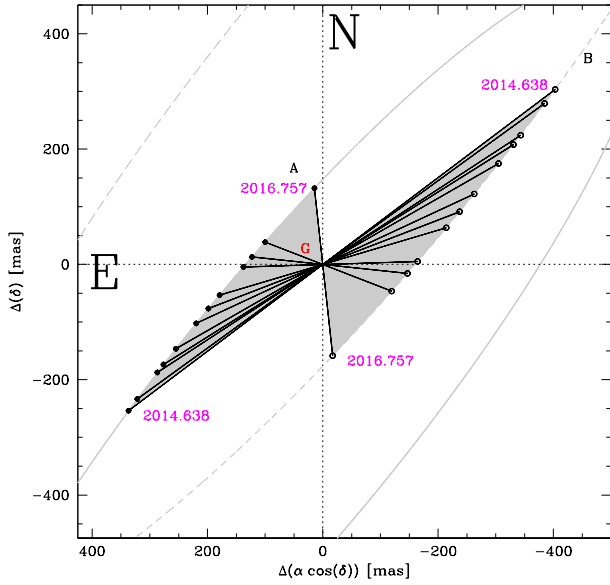


Figure 3. In equatorial coordinates, the positions of A and B components of Luhman 16 relative to our estimate of their common baricenter (indicated with G). We have also indicated the arc of the two baricentric orbits (solid line for A, and dashed line for B) and shaded the orbital area mapped during this *HST* campaign. Note the over 120° covered by the projection of the true anomaly.

with gray regions for both A and B components. For reference, we also show the A-B mass-reduced orbits for the solution derived later in this section. The relative positions, in equatorial coordinates, of Luhman 16 B with respect to Luhman 16 A are shown in Fig. 4 and given in Table 7.

To determine the seven orbital parameters of visual binaries we will follow the trial-and-error approach described by Pourbaix (1994). We employed the two software tools developed and maintained by one of us (D.P.): **union** and **epilogue** (Pourbaix 1998). Practical details about the internal algorithms and some applications are available in Pourbaix (1998a,b, and 2000). Briefly, **union** and **epilogue** are used together to simultaneously adjust the observations of double-lined spectroscopic-visual binaries (VB-SB2). **union** undertakes a global optimization then followed by a preliminary local search. In order to increase the chance of getting the right minimum, the user supplies with a time range to which the orbital period is assumed to belong. **epilogue** processes the results of **union** and generates some statistical information as well as ephemerid for the solution.

The resulting orbital solution for the Luhman 16 A-B system is given in Table 8. To estimate uncertainties we use the conservative approach of permuting the 36 residuals. We give the minimum and maximum values of the different realizations, and their weighted averages. We indicate in the case of ω and Ω that a 5- σ clipping exclude 4 outliers.

Table 7. Cartesian relative equatorial positions of B with respect to A with estimated errors, in mas.

#ID	Julian Year	$\Delta\alpha \cos \delta$ [mas]	$\Delta\delta$ [mas]	σ_Δ [mas]
01	2014.63801	-740.243	557.536	0.319
02	2014.63820	-740.047	557.310	0.319
03	2014.75865	-706.509	513.032	0.383
04	2014.75873	-706.521	512.498	0.348
05	2015.02328	-630.386	411.781	0.335
06	2015.02347	-630.535	411.335	0.373
07	2015.10044	-606.637	381.725	0.352
08	2015.10053	-607.376	381.722	0.343
09	2015.25312	-559.585	321.314	0.266
10	2015.25321	-559.728	321.680	0.321
11	2015.49489	-482.563	224.543	0.333
12	2015.49507	-482.249	224.899	0.326
13	2015.63458	-435.605	168.446	0.297
14	2015.63467	-436.025	168.136	0.332
15	2015.75923	-393.198	117.008	0.342
16	2015.75932	-393.531	116.713	0.376
17	2016.01960	-301.470	9.767	0.342
18	2016.01969	-302.055	9.818	0.385
19	2016.11147	-269.974	-28.218	0.330
20	2016.11167	-269.841	-28.225	0.404
21	2016.24932	-219.280	-84.655	0.449
22	2016.24948	-219.498	-85.021	0.415
23	2016.75726	-31.285	-290.547	0.365
24	2016.75735	-31.701	-291.065	0.398
25	2014.63805	-739.763	556.973	0.193
26	2014.75869	-706.069	512.088	0.273
27	2015.02332	-629.855	411.596	0.249
28	2015.10048	-607.463	380.640	0.211
29	2015.25316	-559.945	320.916	0.247
30	2015.49494	-482.185	224.290	0.252
31	2015.63462	-436.057	167.271	0.179
32	2015.75927	-392.827	116.847	0.247
33	2016.01964	-302.832	9.213	0.313
34	2016.11159	-269.388	-29.052	0.229
35	2016.24936	-219.672	-85.045	0.239
36	2016.75731	-31.870	-290.080	0.221

Table 8. Derived orbital parameters and masses of Luh 16 AB.

parameter	min value	max value	weighted-mean $\pm\sigma$
a [arcsec]	1.69	2.84	1.91 \pm 0.25
a [AU]	3.71	5.67	3.81 \pm 0.50
i [deg]	78.51	80.10	79.21 \pm 0.45
ω [deg]	84	168* (307)	107* \pm 18
Ω [deg]	127.6	132.2* (311)	130.3* \pm 1.1
e	0.31	0.61	0.46 \pm 0.06
P [yr]	24.5	64.4	31.3 \pm 7.9
T_0 [Julian yr]	2016.2	2018.4	2017.1 \pm 0.7
$\mathcal{M}_{\text{tot}}^\dagger$ [\mathcal{M}_\odot]	0.044	0.085	0.056 \pm 0.020
$\mathcal{M}_{\text{tot}}^\ddagger$ [\mathcal{M}_J]	46	89	59 \pm 21
$\mathcal{M}_{\text{Luh A}}^\ddagger$ [\mathcal{M}_J]	26	48	32 \pm 11
$\mathcal{M}_{\text{Luh B}}^\ddagger$ [\mathcal{M}_J]	21	41	27 \pm 10

* 5- σ clipped, rejecting 4 outliers.

Total mass, $^\dagger \mathcal{M}_{\text{tot}} = \mathcal{M}_{\text{Luh 16 A}} + \mathcal{M}_{\text{Luh 16 B}} = a^3/P^2$.

‡ Assuming $q = 0.848$, $\mathcal{M}_{\text{Luh 16 A}} = 1/(1+q)\mathcal{M}_{\text{tot}}$, and $\mathcal{M}_{\text{Luh 16 B}} = q/(1+q)\mathcal{M}_{\text{tot}}$.

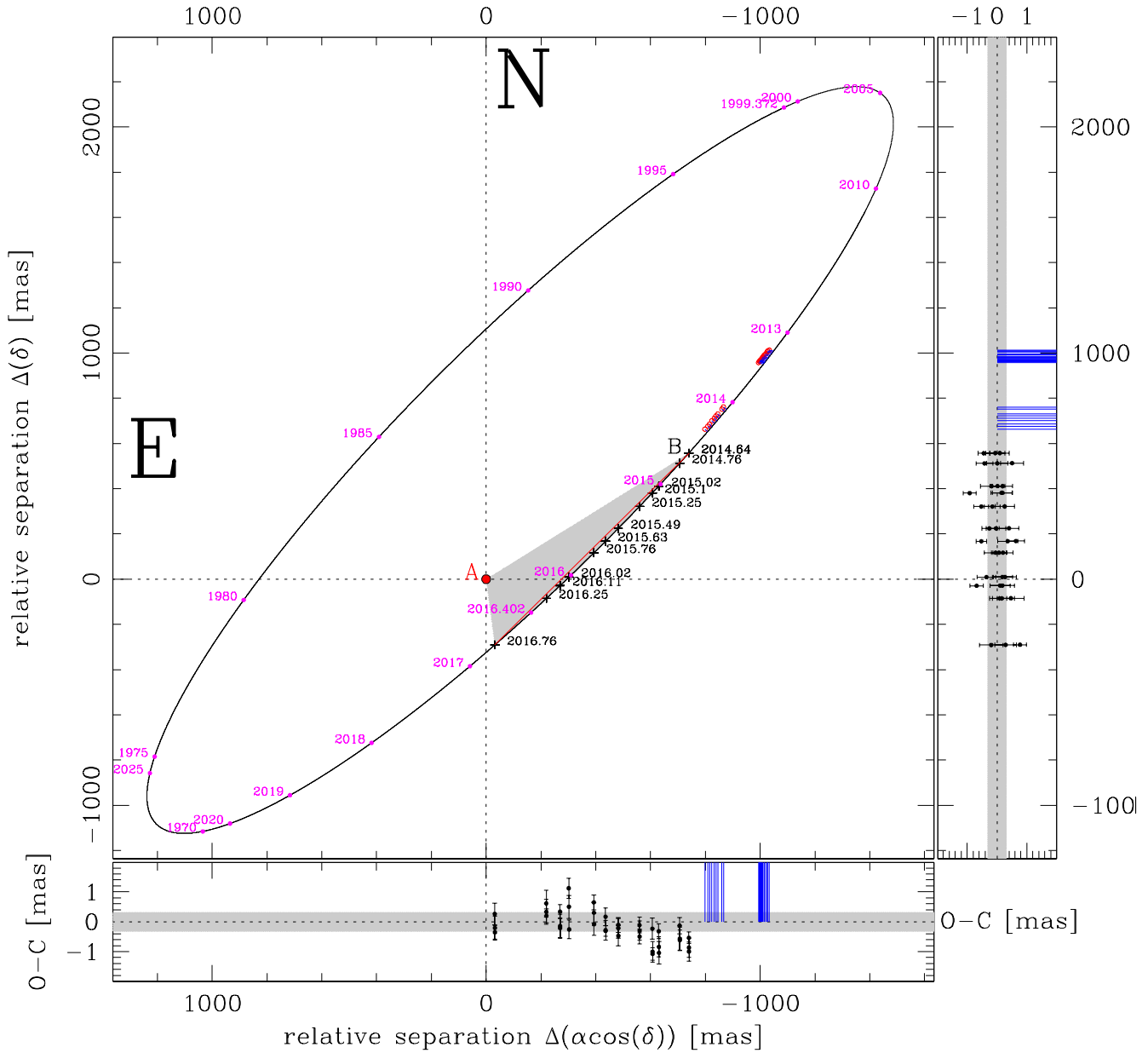


Figure 4. The relative orbit of Luhman 16 B around A. To better highlight the amount of curvature observed with *HST* (+symbols) in the A-B relative orbit, a red line connects the last with the first of the observed relative positions for the B-component. The lower and right panels show in mas the (O–C) residuals with respect to our best orbital model. A gray band is given for reference as the expected uncertainty for any individual positional measurement (0.32 mas). Red circles show the positions available from the Sahlman & Lazorenko 2015, they are all out of scale in the O–C panels. Blue lines connect the individual SL15 data points with their expected positions on our orbital solution at the epoch those observations were collected. See Fig. 5 for a more meaningful comparison of residuals.

5.3 Disagreement with SL15 astrometry

We have downloaded the on-line supporting information available at MNRAS, for Table A1 of the Sahlmann & Lazorenko (2015) study.⁶

⁶ <http://mnras1.oxfordjournals.org/content/453/1/L103/-suppl/DC1>

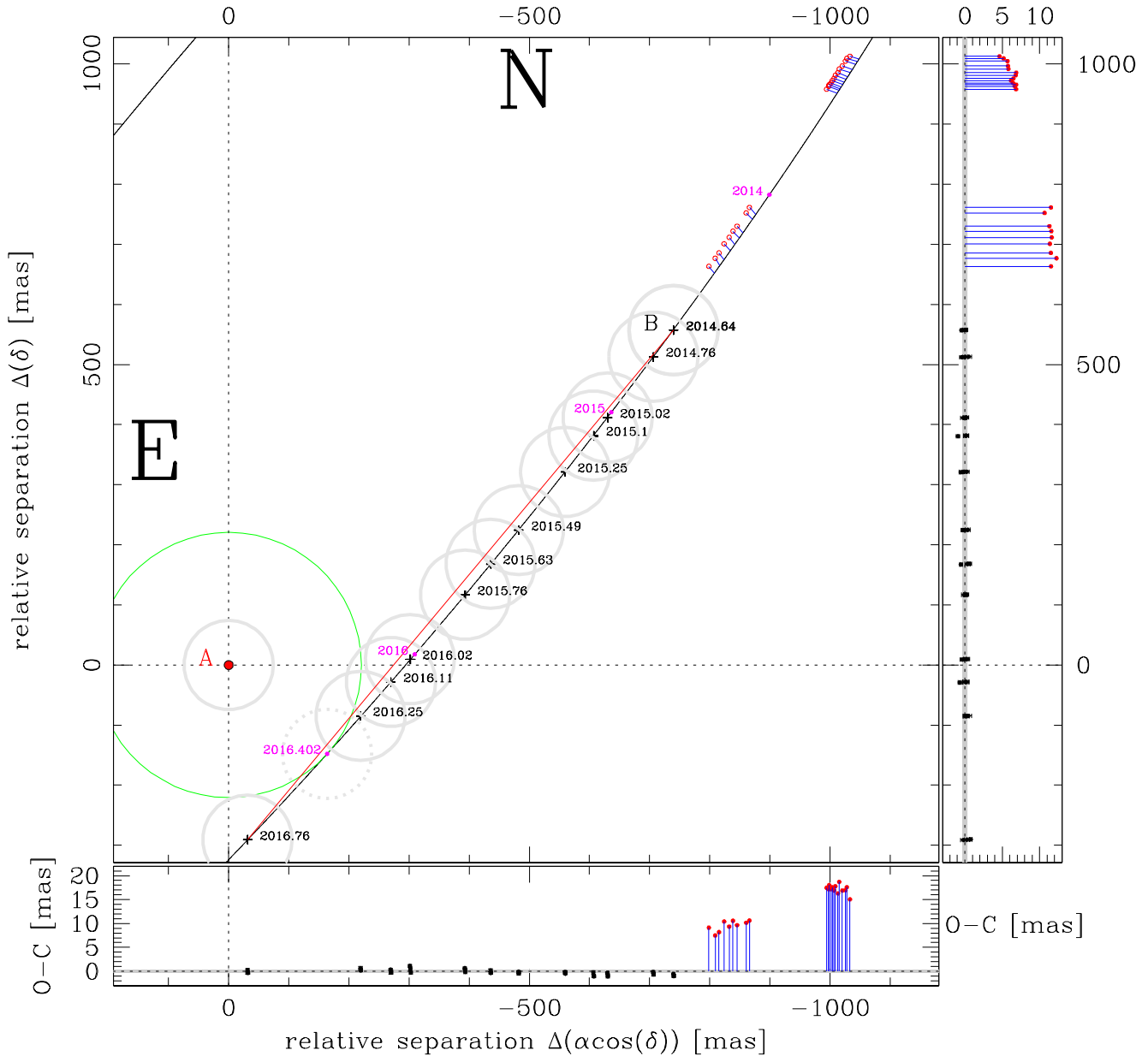


Figure 5. Same as in Fig. 4, only focused on the observed data points from this work and from SL15. The residuals are now shown in a scale that enable to see all residuals of the SL15 data points. Note that neither a simple rotation or shifts, nor a change in the absolute scale can bring into agreement SL15’s *VLT* data points with our *HST*’s data-set. A green circle indicates the apparent periastron (at 220.5 mas) estimated to have happened in 2016.402. For reference, the size of the nominal FWHM with WFC3/UVIS filter F814W (74 mas) is indicated with a gray thick circle at positions where A and B components were observed, and dotted at the not-observed apparent periastron.

This table provides the equatorial coordinates of Luhman 16 A and B collected with FORS2@*VLT* in 22 epochs between April 14 2013 and May 18 2014. The positions are given in the ICRF, after a correction for differential color refraction (DCR) effects was applied.

These data-points could potentially extend by 1.36 years our *HST* data time base-line, resulting in better es-

timates of both astrometric and orbital parameters. Extra monitoring would also improve the search for perturbations induced by third bodies.

We show the relative positions transformed into the tangential plane in Fig. 4 and Fig. 5 as small red circles. Apparently the SL15 data points are not consistent with our orbital solution. We attempt to re-derive the orbital fit includ-

ing also SL15 data but with no success. No simple rotation nor shift can solve the inconsistency. However, if we assume the pixel scale in SL15 to be off by $\sim 5\%$, the data would be nearly aligned with our orbital solution. But, even when this is assumed, and the orbit is re-derived using our *HST* data points and simultaneously including SL15 data points, the results are not physically consistent. In summary, we are unable to fit simultaneously our *HST* data and those by SL15 collected at FORS2@VLT.

In Figure 5 it can be appreciated that while our observed *HST* data points significantly deviate from the straight line (by over 25 mas, at $\sim 100\sigma$) those observed by SL15 are almost consistent with a straight line, deviating no more than very few mas, which seems consistent with the observed amount of scatter in their 22 data points. This is also consistent with the fact that while our *HST* data are exploring over 120° of the projected true anomaly ν , the SL15 data map only a few degrees of ν (see Fig. 4). This is even clearer in Fig. 6, where the amount of curvature traced by our *HST* data is better exposed.

We cannot point to the exact reason(s) of these discrepancies, however, we suspect the usual limitations of ground-based facilities may be responsible, i.e.: (i) the limited parallax factor covered by the ground-based data (see Fig. 3 of SL15); (ii) the FORS2 geometric astrometric stability (camera focal enhancing, de-rotator, active optic stability) and the effects of Earth’s atmosphere on the astrometry (variable PSFs, variable extinction and residual DCR); (iii) the limited angular resolution for this tight binary (~ 1 arcsec during 2013-2014, i.e., comparable to the ground-based seeing); and (iv) the limited arc of the AB orbit the ground-based data cover. SL15 quote positional errors within individual images as low as 0.25 mas, and we suspect that this quoted uncertainty—below the *HST* geometric distortion limit—reflects only internal errors, which might severely underestimate the true (internal and systematic) errors. Nevertheless, their orbital solution, although poorly constrained by the data, still gives (O-C) residuals consistent with their quoted errors. It is also unclear whether in deriving their proper motions they made use of the original WISE AB-photo-center position (of the unresolved components). Instead, we are only using our 2014-2016 *HST* data, as using unresolved position of the photo-center (and at a different wavelength) would surely result in decreasing the accuracy of our solution, biasing our estimates for astrometric parameters of G and q .

6 COMPARISON WITH RADIAL VELOCITIES FROM THE LITERATURE

In deriving the orbit of a visual binary from astrometry only, the inclination (which appears as $\cos i$) is degenerate in i and $-i$ and only radial velocities (RVs) can remove this degeneracy and determine the sign. Thankfully a couple of RVs measurements are available from the literature and *epilogue* and *union* can process RVs (Pourbaix 1998).

The only suitable resolved heliocentric RVs available from the literature are the ones of Kniazev et al. (2013) and Crossfield et al. (2014). Kniazev et al. at epoch 2013.196 give $23.1 \pm 1.1 \text{ km s}^{-1}$ and $19.5 \pm 1.2 \text{ km s}^{-1}$, for components A and B respectively. Crossfield et al. at epoch 2013.342 give

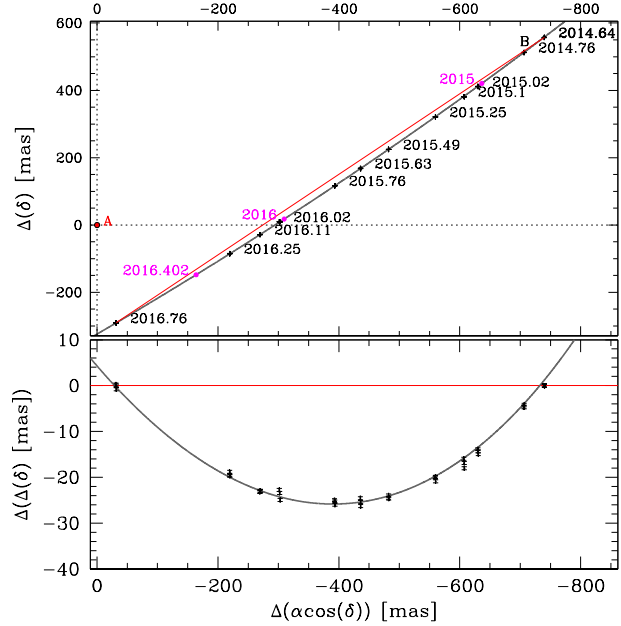


Figure 6. Same as in Fig. 5, only focused on the curvature.

Table 9. Final orbital parameters and masses of Luhman 16 AB.

a [arcsec]	1.91	± 0.25
a [AU]	3.81	± 0.50
i [deg]	-79.21	± 0.45
ω [deg]	287	± 18
Ω [deg]	310.3	± 1.1
e	0.463	± 0.064
P [yr]	31.3	± 7.9
T_0 [Julian yr]	2017.12	± 0.65
\mathcal{M}_{tot} [M_\odot]	0.056	± 0.020
\mathcal{M}_{tot} [M_J]	59	± 21
$\mathcal{M}_{\text{Luh A}}^\dagger$ [M_J]	32	± 11
$\mathcal{M}_{\text{Luh B}}^\dagger$ [M_J]	27	± 10

for $20.1 \pm 0.5 \text{ km s}^{-1}$ and $17.4 \pm 0.5 \text{ km s}^{-1}$, for components A and B respectively.

Inevitably, there are numerous difficulties to estimate the absolute RV zero points of heterogeneous observations collected with different instruments at different telescopes in different sites, and this is particularly true when comparing RVs derived from optical and IR observations. Therefore, as we are interested mainly in the relative RVs of the two components, we assumed the mass ratio q derived in Sect. 5.1, and compute the RVs of the baricenter for the two references. We then impose the velocity of the baricenter in the two data sets to be equal. This was obtained imposing a shift of $+2.6 \text{ km s}^{-1}$ to the Crossfield et al. data.

In Figure 7 we compare our orbital solution with our astrometric data points and with the available radial velocities processed as just described above. From top to bottom, we show our residuals as function of δ , α^* , and RVs. These two RV pairs are sufficient to suggest that i should have a negative value. Consequently also the ω and Ω change by 180° . For clarity the new amended values are given in Table 9.

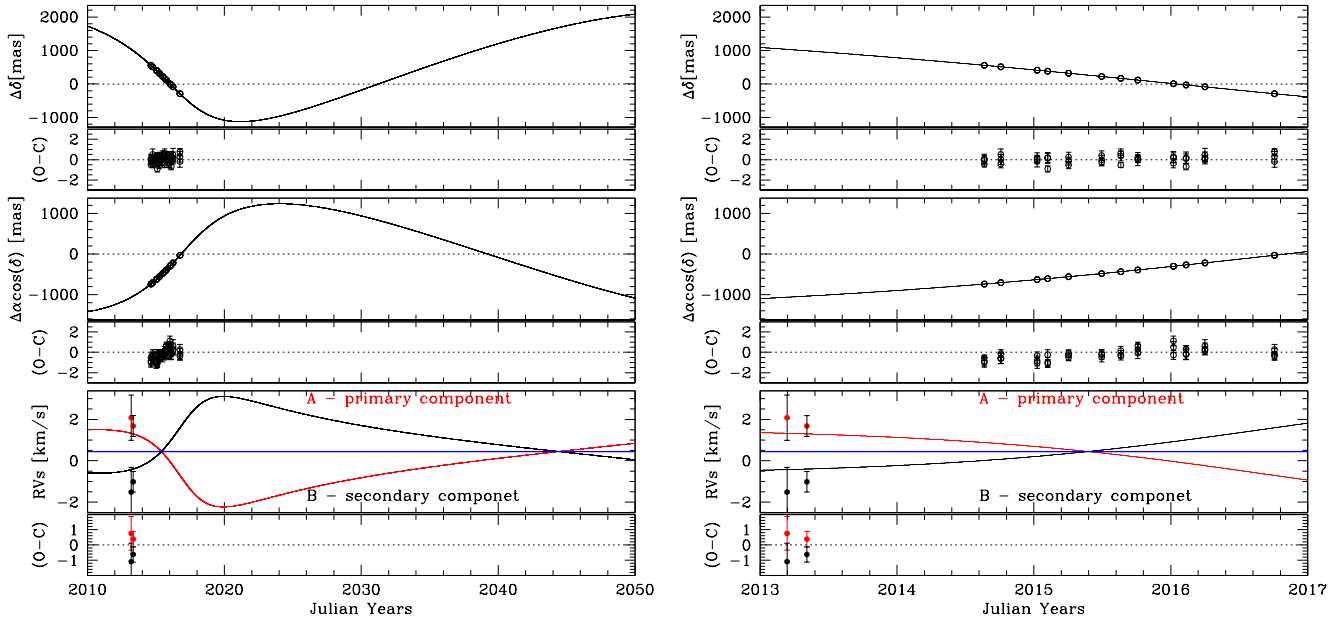


Figure 7. From top to bottom, the three panels show the comparisons between the observed $\Delta(\delta)$, $\Delta(\alpha \cos \delta)$, radial velocities (RVs), and the corresponding quantities from our best orbital fit for the Luhman 16 AB system. Each comparison also shows the Observed – Calculated values below the corresponding panels. The RVs available from literature were processed as described in the text. (*Left:*) We show the models over a full A-B orbital period as reference for the expected full amplitudes of these quantities, although observations are currently limited to just ~ 3.5 yr. (*Right:*) Same plot, but focused just on the time interval where data are actually available so far.

7 PHOTOMETRY

Our *HST* photometry were calibrated to the Vega magnitude system by adding the filter zeropoints ($ZP_{m_{F814W}} = 29.02 \pm 0.02$ and $ZP_{m_{F606W}} = 32.24 \pm 0.02$, following procedures in Bedin et al. 2005)⁷ to the instrumental magnitudes given in Table 5. The absolute accuracy of the calibration is about 0.02 mag per filter. Our observations are not well suited for constraining rotational modulation of these sources, but provide some of the most precise optical photometry for the two brown dwarfs.

In Fig. 8 we summarize the photometry obtained for the targets (Luh 16 A in blue, and B in red) and for the sources in our WFC3/UVIS field (black square symbols). On the left panel we show the $(m_{F606W} - m_{F814W})$ vs. m_{F814W} color-magnitude diagram (CMD). The onset of saturation in the 60 s exposure in F814W is indicated by a dotted line. Note how Luh 16 A and B are considerably redder than any other source in the field, and just below the saturation level (as planned). On the right panels we show our registered and calibrated magnitudes obtained for each image. The error bars associated with each data points is the r.m.s. for stars within 1 magnitude below the saturation level. This is 0.01 for all, with the exception of B in F606W, for which we associate an error of 0.0125 mag. Both Luh 16 components appear to have a scatter considerably larger than field objects of the same magnitudes, in particular the B component.

Luhman 16 B is one of the highest-amplitude variable brown dwarf known (Gillon et al. 2013, Biller et al. 2013, Buenzli et al. 2014, 2015) and spatially resolved studies

discovered variability also in Luhman 16 A (Buenzli et al. 2015) emerging from the rotation of the heterogeneous cloud deck of the brown dwarf. Time-resolved precision photometry by Gillon et al. (2013) showed rapidly evolving light curve variations in Luhman 16 B and multi-band photometry and resolved ground-based spectroscopy by Biller et al. (2013) and Burgasser et al. (2013), respectively, showed wavelength- (and therefore pressure-) dependent phase shifts and amplitude variations. Buenzli et al. (2014, 2015) used high-precision time-resolved *HST* spectroscopy (0.8–1.7 μm range) to show that correlated temperature and cloud thickness variations are responsible for the observed near-infrared spectral evolution, similar to other variable L/T transition brown dwarfs (e.g., Radigan et al. 2012, Apai et al. 2013). Crossfield et al. (2014) presented time-resolved CO line profile observations to derive the first Doppler-imaging map for a brown dwarf, which revealed multiple bright and dark patches; Karalidi et al. (2015) used a Markov Chain Monte Carlo-optimized forward modeling procedure (*Aeolus*, with a finely pixelized sphere and assuming elliptical structures) to derive the simplest surface brightness map that is consistent with the observed variations. Although taken hundreds of rotations apart and with different techniques, the Crossfield et al. and Karalidi et al. maps show some similarity in terms of the approximate size, distribution, and contrasts of the features.

The *observed* variability for component A is 0.11 magnitudes in F606W and 0.08 magnitudes in F814W, while for component B we observed variations as large as 0.11 magnitudes in F606W and 0.25 magnitudes in F814W. These are significantly larger than the ~ 0.01 photometric precision

⁷ and zero points at http://www.stsci.edu/hst/wfc3/phot_zp_lbn

of our measurements. As our observations are not resolved on the timescale of the rotational periods of Luhman 16 A and B, we cannot derive peak-to-peak changes for the objects, therefore the reported values should be considered lower limits on the intrinsic amplitudes at these wavelengths. Red-optical variability has been detected in other T dwarfs (e.g., Gillon et al. 2013; Heinze et al. 2015), which suggests that cloud amplitudes are likely as large if not larger in the red optical than they are in the near-infrared (1-1.6 μm) bands, potentially providing stronger constraints on condensate grain size distribution (e.g., Lew et al. 2016).

Alternately, variability of nonthermal emission induced by magnetic activity could be responsible for this signal, as such emission has a much greater relative impact at optical wavelengths where the photospheric emission is weak (e.g., Croll et al. 2016; Gizis et al. 2017). Magnetic emission has been detected from T dwarfs at optical (e.g., Burgasser et al. 2003; Kao et al. 2016; Pineda et al. 2016) and radio wavelengths (e.g., Route & Wolszczan 2012, 2016); however, neither component of Luhman 16 AB was found to exhibit $H\alpha$ emission to an equivalent width limit of 1.5 \AA (Faherty et al. 2014), and the system was undetected in single-epoch radio and X-ray observations (Osten et al. 2015). Further investigation into the variability of this system, over broad wavelength and time spans, is certainly warranted.

Our observations are also consistent with the extended base-line (spatially unresolved) photometric monitoring of the Luhman 16 AB system in the Pan-STARRS-Z band and in the SDSS i' band, which show that modulations 0.05 magnitude are typical over the timescales of the rotational period, but these authors also report changes as large as 0.1 mag (Street et al. 2015).

8 PRESENCE OF EXOPLANETS

The main goal of this project is to search for, and possibly to characterize, exoplanets and other bodies, in P-type or S-type orbits around the Luhman 16 A and B components. We summarize the results of this preliminary work as follow:

(1) We inspected each epoch for faint companions, and find no detectable third body co-moving with the Luhman 16 A-B system within our WFC3/UVIS field of view. At 2 pc, our search area extends from 1 AU ($0''.5$) to 80 AU. Assuming a detection limit of $m_{F814W}=23$ magnitudes (Fig. 8), we can rule out well-resolved companions to an absolute magnitude limit of $M_{F814W} \approx 26.5$. For comparison, the T9 dwarf UGPS J072227.51-054031.2 has an absolute i -band magnitude of 26.2 (Leggett et al. 2012), so these observations rule out companions warmer than a Y dwarf ($T_{\text{eff}} \gtrsim 500 \text{ K}$). It appears that these new *HST* images do not provide any new constraints (from direct detection) that surpass those from Melso et al. (2015).

In Fig. 9 we show the amplitude of the expected astrometric perturbation for a number of cases, over-imposed on our current 3σ threshold. For simplicity, we assume circular planetary orbits as these are more likely to be stable, and adopt the maximum and minimum masses for Luh 16 A and Luh 16 B, respectively, given in Table 8.

(2) Using our *HST*-only data, we confirm the results by SL15 as we also do not see any significant residual in our

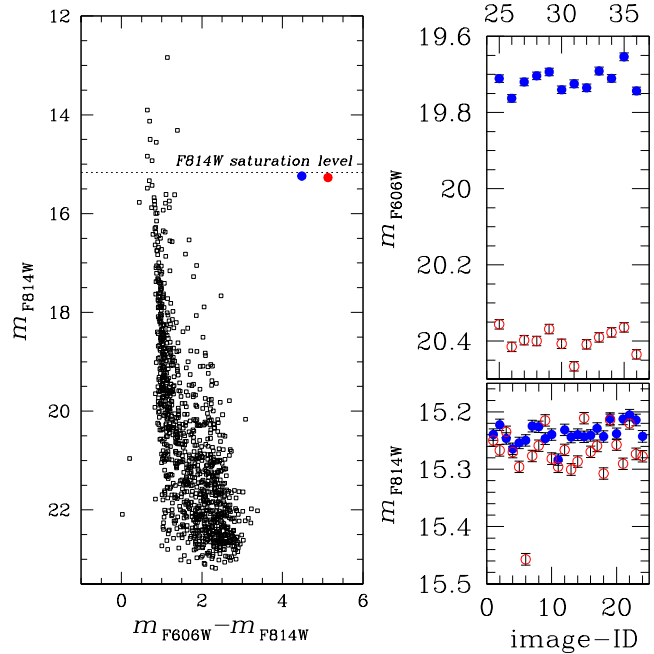


Figure 8. Summary of the photometric data released as part of this work. Black symbols are field objects observed within our WFC3/UVIS field, Luh 16 A is indicated in blue and Luh 16 B in red. On the left panel we show the CMD of all the sources. A dotted line indicate the on-set of saturation. On the right panels we show the individual magnitudes for Luh 16 A and B (F606W on top, and F814W on bottom), as measured in each of the 36 images used in this work, as function of the image #ID (Table 1).

motions at the \sim mas level compatible with the perturbation induced by a third body having a mass larger than 2 Jupiter Masses (\mathcal{M}_J), and period between 20 days and 300 days.

(3) Our longer time base-line of 2.12 yrs, compared to the SL15 base-line of 1.09 yrs, allow us to exclude the presence of $2\mathcal{M}_J$ planets with period as long as 2 yrs.

(4) We can also exclude the presence of $1\mathcal{M}_J$ with period between 20 days and 2 years.

(5) Finally, we can extend this claim down to significantly lower masses, i.e., down to Neptune masses for periods longer than about 1 year.

To increase sensitivity and place a lower limit to what we could detect, we can average the residuals before and after 2015.75, where there might seem to be a marginally significant residual of about $0.5 \pm 0.2 \text{ mas}$ (mainly in α^*). Even assuming that this can be ascribed to a genuine signature caused by a third body—rather than a more likely effect of residual systematic errors—and assuming masses between the maximum and minimum masses for Luh A and B, it would imply a period larger than 2 years and a mass not greater than one Neptunian mass.

(6) Neither a simple shift, nor a rotation, nor a scale change can reconcile our *HST*-derived positions with those by SL15 based on data obtained with *VLT* from ground. The two data sets can *not* be fit with a common orbital solution unless an *ad-hoc* third body is used to explain that discontinuity; a possibility that at this stage we have not explored.

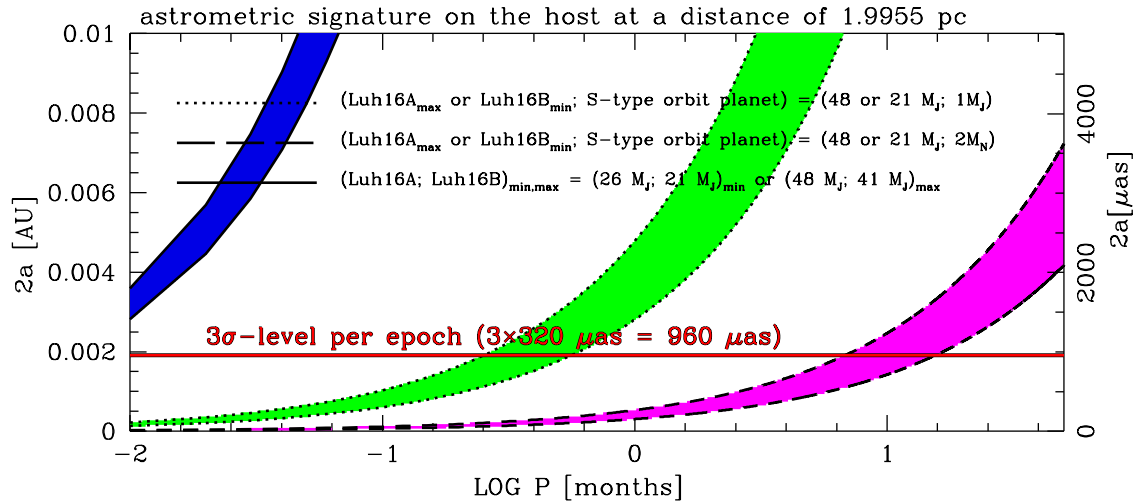


Figure 9. Assuming a distance of 1.9955 pc for Luhman 16 AB, and the maximum and minimum masses for Luh 16 A and Luh 16 B derived in Table 8, respectively, we show the relation between twice the semi-major axis $2a$ of the barycentric orbit of the luminous companions (A or B) around the center of mass with a non-luminous planet, and the period (P). Dotted lines show this relation for a planet with a mass of $1 M_{\text{Jupiter}}$. The green region indicates the loci for intermediate masses for A or B. The dashed lines (and corresponding region in magenta) indicate the corresponding astrometric signal induced by a $2 M_{\text{Neptune}}$ exoplanets. For reference, the solid lines (and blue region) show the amount of A-B orbital motion if the system was on a circular orbit. Twice the semi-major axes because that is the maximum size of the total range of motion for a circular orbit that we can measure. The horizontal red line sets our limit to the astrometric signal, i.e., $3\sigma \simeq 960 \mu\text{as}$, or, for a distance of ~ 2 pc, equivalent to ~ 0.002 AU (i.e., about 300 000 km).

9 ELECTRONIC MATERIAL

As part of this work, we electronically release as supplementary material on the Journal: *i*) The individual observed positions and magnitudes for A and B in the tables. *ii*) The astrometrized stack of the *HST* observations in filter F814W. *iii*) The photometry for the field objects.

10 CONCLUSIONS

In this paper we presented the first results from an ongoing, high-precision, *Hubble Space Telescope*-based astrometric monitoring campaign targeting the Luhman 16 AB system, the closest brown dwarfs to the Sun. The key findings of our study are as follows:

(i) We rule out co-moving companions down to Y dwarf spectral types in the range 1-80 AU. This result confirms the finding of Melso et al. (2015), which is based on superior data for this analysis. Note that Melso et al. also extended this investigation at wider separations.

(ii) Our *HST* data alone confirm the results by SL15: we find no evidence for \sim mas-level residuals that would be consistent with an exoplanet in the system with a mass greater than $2 M_{\text{Jup}}$ and with a period between 20 and 300 days.

(iii) We extend this results to lower masses and larger periods. In particular no exoplanets with masses larger than a Neptunian mass and period between 1 year and 2 years.

(iv) Our measurements significantly improve the parallax and proper motion of the Luhman 16 AB system, and indicates that this system is closer to the Sun (< 2 pc) than previous measurements.

(v) We have also improved on the mass ratio q of the Luhman 16 AB system and mapped the motions through the apparent periastron.

Further significant improvements on the astrometric solution and parallax of the Luhman 16 AB system can be made in the near-future: We plan to focus on the trailed *HST* images already collected and those planned for August 2018, to further improve the astrometric precision and search exoplanets down to few Earth masses. Follow-up observations with the VLT/CRIRES+ instrument will provide accurate radial velocity data, an important complement to our 2-D astrometric data, as it will provide the missed component necessary for the complete tri-dimensional picture of the kinematic in the system. In addition, the Gaia DR2 dataset will provide absolute motions, positions, and distances of several stars in the field, allowing us to link our positions to an absolute system.

11 ACKNOWLEDGMENTS

We thank an anonymous referee for the critical and careful reading of our manuscript, and for her/his suggestions and corrections that have contributed to improve this work. D.A. and A.B. acknowledge support from STScI grants GO-13748 and GO-14330. We warmly thank Shelly Meyett and Peter McCullough at STScI, our Program Coordinator and Contact Scientist for their great support during the planning of the multi-year observations.

REFERENCES

- Anderson J. & King I. R., 2006, Instrument Science Report ACS 2006-01, STScI, Baltimore
- Anderson J. et al. 2007, Instrument Science Report ACS 2007-08, STScI, Baltimore
- Anderson, J. et al. 2008, AJ, 135, 2055

- Anderson, J. & Bedin L. R. 2010, *PASP*, 122, 1035
- Apai, D. et al. 2005, *Science*, 310, 834
- Apai, D. et al. 2013, *ApJ*, 768, 121
- Bedin, L. R. et al. 2003, *AJ*, 126, 247
- Bedin, L. R., Cassisi, S., Castelli, F., Piotto, G., Anderson, J., Salaris, M., Momany, Y., & Pietrinferni, A. 2005, *MNRAS*, 357, 1038
- Bedin, L. R. et al. 2014, *MNRAS*, 439, 354
- Bellini, A. & Bedin L. R. 2009, *PASP*, 121, 1419
- Bellini, A., Anderson, J., Bedin, L. R. 2011, *PASP*, 123, 622
- Bellini, A. et al. 2013, *ApJ*, 769, 32
- Biller, B. A. et al. 2013, *ApJ*, 778L, 10
- Boffin, H. M. et al. 2014, *A&A*, 561, L4
- Buenzli, E. et al. 2014, *ApJ*, 782, 77
- Buenzli, E. et al. 2015a, *ApJ*, 798, 127
- Buenzli, E. et al. 2015b, *ApJ*, 812, 163
- Burgasser, A. J. et al. 2003, *ApJ*, 594, 510
- Burgasser, A. J. et al. 2013, *ApJ*, 772, 129
- Burrows, A., Hubbard, W. B., Lunine, J. I. & Liebert, J. 2001, *Reviews of Modern Physics*, 73, 719
- Casertano, S. et al. 2016, *ApJ*, 825, 11
- Cox C., Gilliland R. L., 2003, in Arribas S., Koekemoer A., Whitmore B., eds, *The 2002 HST Calibration Workshop: Hubble after the Installation of the ACS and the NICMOS Cooling System*. STScI, Baltimore, p. 58
- Crossfield, I. J. M. et al. 2014, *Nature*, 505, 654
- Croll, B. et al. 2016, arXiv:1609.03586
- Dressel, L., 2017. "Wide Field Camera 3 Instrument Handbook, Version 9.0" (Baltimore: STScI)
- Dressing, C. D. & Charbonneau, D. 2013, *ApJ*, 767, 95
- Faherty, J. K. et al. 2014, *ApJ*, 790, 90
- Fressin, F. et al. 2013, *ApJ*, 766, 81
- Gatewood, G. & Eichhorn, H. 1973, *AJ*, 78, 769
- Gatewood, G. 1974, *AJ*, 79, 52
- Gillon, M. et al. 2013, *A&A*, 555L, 5
- Gillon, M. et al. 2017, *Nature*, 542, 456
- Gizis, J. E. et al. 2017, *ApJ*, 838, 22
- Hayashi, C. & Nakano, T. 1963, *Progress of Theoretical Physics*, 30, 460
- Heinze et al. 2015 *ApJ* 801, 104
- Karalidi, T. et al. 2015, *ApJ*, 814, 65
- Kao, M. M. et al. 2016, *ApJ*, 818, 24
- Kaplan, G, Bartlett, J., Monet, A., Bangert, J. & Puatua, W., 2011, *User's Guide to NOVAS Version F3.1*, (Washington, DC: USNO).
- Kniazhev, A. Y. et al. 2013, *ApJ*, 770, 124
- Kumar, S. S. 1962, *ApJ*, 579, 67
- Lazorenko, P. F. et al. 2011, *A&A*, 527, 25
- Lew et al. 2016 *ApJ* 829, 32
- Leggett, S. K. et al. 2012, *ApJ*, 748, 74
- Lippincott, S. L. 1960, *AJ*, 65, 349
- Lodieu, N. et al. 2015, *A&A*, 581, 73
- Luhman, K. L. et al., 2008, *ApJ*, 688, 362
- Luhman, K. L. 2013, *ApJ*, 767L, 1
- Mamajek, E. E. 2013, arXiv: 1303.5345
- Marquardt, D. W. 1963, *An Algorithm for Least-Squares Estimation of Nonlinear Parameters*, *SIAM J.*, 11, 431
- McCullough, P., MacKenty, J., 2012, *Instrument Science Report WFC3 2012-08*, Hubble Space Telescope, Space Telescope Science Institute, STScI
- Melso, N. D., Kaldon, K. M. & Luhman, K. L. 2015, *AJ*, 150, 62
- Moré, J. J., Garbow, B. S. & Hillstom, K. E. *User Guide for MINPACK-1*, Argonne National Laboratory Report ANL-80-74, Argonne, Ill., 1980
- Mulders, G. D., Pascucci, I., Apai, D. 2015, *ApJ*, 798, 112
- Mulders, G. D., Pascucci, I., Apai, D. et al. 2016, *AJ*, 152, 187
- Osten, R. A., Melis, C., Stelzer, B. et al. 2015, *ApJL*, 805, L3
- Pascucci, I. et al. 2016, *ApJ*, 831, 125
- Pascucci, I. et al. 2009, *ApJ*, 696, 143
- Pineda, J. S. et al. 2016, *ApJ*, 826, 73
- Pourbaix, D. 1994, *A&A*, 290, 682
- Pourbaix, D. 1998a, *A&AS*, 131, 377
- Pourbaix, D. 1998b, on 'Orbit determination of binary stars using simulated annealing', in 'High performance software for non-linear optimization: status & perspective'. Eds. R. De Leone, A. Murli, G. Toraldo and P.M. Pardalos, Kluwer Academic Publishers
- Pourbaix, D. 2000, in 'Encyclopedia of optimization', Eds. C.A. Floudas and P.M. Pardalos, Kluwer Academic Publishers
- Pravdo, S. H. & Shaklan, S. B. 2009, *ApJ*, 700, 623
- Radigan, J. et al. 2012, *ApJ*, 750, 105
- Ricci, L. et al. 2013, *ApJ*, 764L, 27
- Riess, A. G. et al. 2014, *ApJ*, 785, 161
- Robin, A. C. et al. 2004, *A&A*, 416, 157
- Route, M. & Wolszczan, A. 2012, *ApJ*, 747L, 22
- Route, M. & Wolszczan, A. 2016, *ApJ*, 821L, 21
- Sahlmann, J. & Lazorenko, P. F., 2015, *MNRAS*, 453, 103L, SL15
- Street et al. 2015 *ApJ* 812, 161
- The Gaia Collaboration*, 2016, *A&A*, 595, 2
- Ubeda L., Kozhurina-Platais V., Bedin L. R., 2013, Technical report, ACS/WFC Geometric Distortion: a time dependency study
- van de Kamp, P. & Lippincott, S. L. 1951, *AJ*, 56, 49
- van de Kamp, P. 1963, *AJ*, 68, 515
- van de Kamp, P. 1969, *AJ*, 74, 238
- van de Kamp, P. 1967, *Principle of Astrometry*, W.H. Freeman and company